Spreading of α-synuclein rewires organelle communication and disrupts neuron-astrocyte mitochondrial quality control

Melissa Birol

Melissa.Birol@mdc-berlin.de

Berlin Institute of Medical Systems Biology (BIMSB), Max Delbrück Center for Molecular Medicine https://orcid.org/0000-0003-3397-8446

Elisabeth Fritsch

Berlin Institute of Medical Systems Biology (BIMSB), Max Delbrück Center for Molecular Medicine https://orcid.org/0000-0002-4207-0395

Kamelija Horvatovic

Berlin Institute of Medical Systems Biology (BIMSB), Max Delbrück Center for Molecular Medicine

Paula Santos Otte

Berlin Institute of Medical Systems Biology (BIMSB), Max Delbrück Center for Molecular Medicine

Tomas Koudelka

Kiel University

Jana Rossius

Max Delbrück Center for Molecular Medicine https://orcid.org/0009-0000-6011-9714

Caroline Braeuning

Berlin Institute for Medical Systems Biology (BIMSB), Max Delbrück Center for Molecular Medicine in the Helmholtz Association (MDC), Berlin Institute of Health (BIH) https://orcid.org/0009-0007-1439-9920

Laura Breimann

Department of Genetics, Harvard Medical School

ilaria Piazza

MDC Berlin https://orcid.org/0000-0001-5895-6134

Article

Keywords:

Posted Date: July 29th, 2026

DOI: https://doi.org/10.21203/rs.3.rs-10396187/v1

Additional Declarations: There is **NO** Competing Interest.

Article

Spreading α-synuclein rewires organelle communication and impairs neuron–astrocyte mitochondrial quality control

Elisabeth Fritsch[1,2], Kamelija Horvatovic[1#], Paula Santos Otte[1#], Tomas Koudelka[3], Jana Rossius[1], Caroline Braeuning[4], Laura Breimann[5], Ilaria Piazza[3,6,7], Melissa Birol[1]*

[1] Laboratory for Single Molecule Biophysics probing Quantitative Neuroscience, Berlin Institute of Medical Systems Biology (BIMSB), Max Delbrück Center for Molecular Medicine, 10115 Berlin, Germany
[2] Institute of Chemistry and Biochemistry, Freie Universität Berlin, Berlin, Germany
[3] Max-Delbrück-Center for Molecular Medicine in the Helmholtz Association (MDC), Berlin, Germany.
[4] Genomics Technology Platform, Max Delbrück Center for Molecular Medicine in the Helmholtz Association, Berlin, Germany and Berlin Institute of Health at Charité – Universitätsmedizin Berlin, Core Unit Genomics
[5] Department of Genetics, Harvard Medical School, Boston, MA 02115, USA
[6] Science for Life Laboratory, Department of Molecular Biosciences, The Wenner-Gren Institute, Stockholm University, Stockholm, Sweden
[7] Department of Microbiology, Tumor and Cell Biology, Karolinska Institutet, Solna, Sweden

# Equal contribution
* Correspondence should be addressed to:
Melissa Birol (Melissa.birol@mdc-berlin.de)

Abstract

Progressive intercellular spreading of α-synuclein (αS) is implicated in pathology initiation and propagation of synucleinopathies. However, how recipient neurons respond to incoming αS and whether these responses contribute to disease-associated early metabolic events, remains unknown. Here, using extracellular monomeric αS to model the earliest cellular response to spreading, we found that internalized αS accumulates at tri-organelle contact sites linking mitochondria, endoplasmic reticulum, and endo/lysosomal compartments. At these interfaces, αS stabilizes generally dynamic contacts and constrains their remodeling, thereby rewiring organelle communication. These effects require the acidic αS C-terminus and are not recapitulated by intracellular αS overexpression. Proteomic profiling of αS-associated mitochondria identified a contact site-enriched but quality-control-deficient state. Functionally, spreading αS impairs neuron-astrocyte mitochondrial quality control (MQC) by reducing neuronal mitochondria transfer to astrocytes, while enhancing mitochondrial import. Our findings establish organelle contact sites as critical target of spreading αS, through which rewired organelle communication impairs MQC and neuron-astrocyte crosstalk.

Introduction

The propagation of pathogenic proteins between cells is increasingly recognized as a fundamental process in neurodegenerative diseases[1,2]. In synucleinopathies, α-synuclein (αS) spreads through interconnected neural circuits and is thought to contribute to the initiation and progression of pathology[3–5]. Both monomeric and pathological forms of αS spread between cells[4,6,7], exploiting routes such as tunneling nanotubes, exosomes, and receptor-mediated endocytic uptake to move from neuron to neuron or from neurons to glial cells[8–12]. Consistent with this αS is detected in cerebrospinal fluid (CSF) under both physiological and pathological conditions[13,14], indicating that neurons continuously release αS into the extracellular space. Such secretion may either confer specific biological functions or serve as a clearance route to prevent aggregation, whereas reuptake by neighboring cells may drive disease progression. Basal extracellular αS levels in CSF are typically reported in the low nanogram-per-milliliter range, although absolute concentrations vary across studies and detection assays used[14,15]. In synucleinopathies, the total CSF αS is typically reduced, whereas oligomeric and phosphorylated species increase[16], changes thought to reflect the sequestration of αS into intracellular aggregates. Once internalized, oligomeric and fibrillar αS species can overwhelm intracellular homeostasis, particularly the autophagy-lysosome system, leading to further accumulation and cellular stress[17,18]. In parallel, glial cells such as astrocytes and microglia respond to extracellular αS by releasing pro-inflammatory cytokines that aggravate neuronal dysfunction[19–21]. While these αS species are established drivers of proteostatic stress, much less is known about the effects of monomeric αS that is continuously exchanged between cells under physiological and pathological conditions. Whether monomeric αS transfer alone can reshape cellular organization and homeostasis is unknown. Addressing this question is essential for defining the earliest cellular consequences of αS spreading and identifying mechanisms that may predispose recipient cells to later dysfunction.

Mitochondrial dysfunction is among the earliest and most prominent features of synucleinopathies[22–25]. In these disorders, αS impairs mitochondrial function[26] and co-accumulates with mitochondria within Lewy bodies[27]. Disruption of mitochondrial dynamics leads to energy deficits, oxidative stress, and excessive production of reactive oxygen species (ROS), thereby accelerating neuronal degeneration[26,28–30]. Beyond intrinsic defects, mitochondrial function depends on coordinated communication with other organelles, including the endoplasmic reticulum (ER)[31–33] and the endolysosomal system[34,35]. These interactions are

mediated through specialized membrane contact sites, including mitochondria-associated membranes (MAMs), which integrate lipid transfer, calcium signaling, and mitochondrial dynamics and are increasingly recognized as key regulators of mitochondrial quality control (MQC)[36–38]. Moreover, controlled cell-to-cell communication has recently been shown to be crucial for MQC[39–41], highlighting the interplay between intra- and intercellular mechanisms that sustain mitochondrial function. Notably, αS has been reported to associate with MAMs and to modulate ER–mitochondria communication[42–45]. In Parkinson's disease (PD), both rare familial mutations and common genetic risk variants converge on the endolysosomal system and mitochondria as key mediators of cellular dysfunction and neurodegeneration. Genes such as LRRK2, GBA1, VPS35, and ATP13A2 regulate endolysosomal homeostasis, whereas PINK1 and PRKN control mitophagy[46,47].

Mitochondria themselves can be exchanged between cells, a process known as mitochondrial transfer[41,48]. Damaged or dysfunctional mitochondria can be replaced by intact mitochondria from healthier cells, promoting cell survival and function[41,49,50]. Stressed cells can extrude damaged mitochondria that are then taken up and degraded by recipient cells[39,40]. Mitochondrial transfer allows cells to share bioenergetic capacity, compensate for impaired ATP production, mitigate oxidative stress, and restore mitochondrial function in compromised cells. This process has been observed in tissue repair[50], immune responses[51], and diseases such as cancer[52,53], cardiovascular disorders[40], and, more recently, in neurodegeneration[54,55]. In the brain, glial cells play a key supportive role in maintaining neuronal health and homeostasis[56]. Under mitochondrial stress, neurons can extrude dysfunctional mitochondria via tunneling nanotubes or vesicular pathways, and neighboring astrocytes can engulf these mitochondria and degrade them through their own lysosomal machinery[39]. This process depends on coordinated mitochondrial dynamics, vesicular trafficking, and organelle contact-site signaling. This intercellular MQC mechanism enables neurons to offload compromised mitochondria, preventing the accumulation of ROS and progressive mitochondrial failure. Whether the spreading of αS interferes with these mechanisms remains unknown.

To determine whether spreading αS interferes with intracellular and intercellular MQC mechanisms, we investigated how recipient neurons respond to incoming αS. Using extracellular monomeric αS to model early spreading-associated uptake, we found that internalized αS accumulates at organelle contact sites linking mitochondria, the ER, and the endolysosomal system, where it stabilizes normally dynamic MAM-endosome contacts and constrains their remodeling. Quantitative imaging, analyses of organelle dynamics, and proteomic profiling further revealed that αS selectively remodels contact site-associated mitochondrial subpopulations, promoting a contact site-enriched but quality control-deficient mitochondrial state characterized by altered organelle communication and impaired MQC. Functionally, these changes compromise neuron–astrocyte MQC by reducing the transfer of damaged neuronal mitochondria to astrocytes while enhancing compensatory mitochondrial delivery from astrocytes to neurons under stress conditions. Together, our findings establish a mechanistic link between αS spreading, organelle communication, and intercellular mitochondrial homeostasis, providing insight into how early αS transfer initiates cellular dysfunction in synucleinopathies.

Results

Spreading αS localizes on mitochondria-ER-endo/lysosomal contacts

The spread of αS across neurons is thought to involve its trafficking through interconnected organellar networks, yet how internalized αS engages specific subcellular compartments remains unclear. To define

αS intracellular localization upon spreading, iPSC-derived dopaminergic neurons (DNeurons) and SH-SY5Y cells were conditioned with monomeric ATTO 700-labeled αS, at concentrations of 80 nM (denoted αS) and 250 nM (denoted $αS_D$) for 14 h, unless otherwise indicated. These concentrations were selected to assess dose-dependent effects on intracellular targeting while remaining non-toxic to neurons over the experimental time course[11]. Although higher than αS levels typically detected in CSF[14,15], these concentrations were used to model localized exposure in recipient cells upon intercellular transfer. Following internalization, αS accumulated as discrete puncta that localized predominantly at the termini of mitochondrial tubules (Fig. 1a and S1a). Line-profile analyses confirmed that αS puncta resided adjacent to, but rarely overlapped with, mitochondrial tubules (Fig. 1b and S1b). We next performed fluorescence-activated organelle sorting (FAOS) of cell lysates obtained from cells conditioned with αS or $αS_D$ (Fig. 1c). Using MitoTracker Green FM and Alexa Fluor 647-labeled αS, we resolved and quantified distinct mitochondrial subpopulations co-sorting with αS and $αS_D$. This revealed a significant dose-dependent increase in mitochondrial association, with approximately 3.93 ± 0.99% and 7.47 ± 0.50% of total mitochondria events detected for αS and $αS_D$, respectively (Fig. 1c, S1c-e). These data demonstrate that a defined subset of mitochondria associates with internalized αS.

Consistent with this, mitochondria-associated αS puncta frequently appeared within endosomal compartments, suggesting receptor-mediated endocytosis as the principal uptake pathway[10,11]. We found that mitochondria-adjacent αS puncta were often detected at endosomal compartments in SH-SY5Y cells and in DNeurons (Fig. 1d and S1f). Line intensity profiles revealed substantial overlap between αS and LysoSensor-positive endo/lysosomal compartments that reside in proximity to mitochondria (Fig. 1e and S1g). Given that the acidic C-terminal domain of αS regulates membrane interactions, we next tested its contribution to endolysosomal association using a truncated variant comprising residues 1-100 (denoted $αS_{100D}$), applied at 250 nM to match the $αS_D$ condition. To determine whether αS preferentially associates with specific endolysosomal subpopulations or alters organelle acidification, we quantified LysoSensor fluorescence intensity at the level of individual compartments. LysoSensor intensity was used to assess endolysosomal acidity, enabling comparison between the total endolysosomal population (Fig. S1h) and the subset associated with αS (Fig. S1i). αS-localized compartments were modestly enriched within the more acidic range, however, the overall distribution was not shifted across conditions (Fig. S1h, i). While $αS_D$ displayed a broader distribution and $αS_{100D}$ a more constrained profile, the overall tendency remained unchanged. To assess whether αS spreading alters the composition of the endolysosomal pool, we quantified early (Rab5) and late (Lamp1) endosomal markers. Their relative abundance remained unchanged, indicating that αS does not shift the balance between early and late compartments (Fig. 1f).

Endosomes communicate with mitochondria through ER-defined contact sites known as MAMs[57,58], and notably, αS has been reported to associate with MAMs[42–45]. Together, this raises the possibility that spreading αS accumulates at interfaces coordinating endolysosomal–mitochondrial crosstalk. To test this, SH-SY5Y cells expressing the split-GFP-based MAM contact-site reporters ($SPLICS_S$-$P2A^{ER–MT}$, to detect interactions over the range of ~8-10 nm[59]) were treated with αS and imaged. Internalized αS localized to SPLICS-positive puncta that overlapped with the MAM tether protein VAPB (Fig. 1g, h and S1j-m). Colocalization across αS-treated conditions was confirmed by fluorescence intensity line profiles and object-based colocalization analysis (Fig. 1h, i and S1k, m, n). Measurement of the fraction of total αS overlapping MAMs (M1) revealed comparable enrichment for αS and $αS_D$, with approximately 20% of total αS puncta associated with MAMs. In contrast, $αS_{100D}$ exhibited a reduction in MAM-associated αS signal (Fig. 1i and S1n). When normalized to total MAMs (M2), all αS variants occupied a substantial fraction

(>60%) of available MAM structures. These data suggest that αS engages MAMs as part of its intracellular trafficking route, with the C-terminus modulating its relative enrichment at these interfaces. We next asked whether αS association alters MAM architecture. Quantification of contact-site density revealed an increase in MAM number across all αS conditions compared with control cells (Fig. 1j). Although mean MAM size was unchanged (Fig. S1o), size-distribution analysis revealed a shift toward smaller contact areas, most prominently in αS_D. These findings demonstrate that αS not only localizes to MAMs but also actively remodels contact-site architecture, positioning these interfaces as key sites of αS-mediated organelle regulation.

Spreading αS alters the dynamic remodeling of MAM-endosome contacts

Organelle contact sites occupy a small fraction of total membrane surface yet play essential roles in lipid, ion, and metabolite exchange[60]. These contacts are highly transient, continuously forming and resolving to maintain organelle communication. We hypothesized that αS recruitment to MAM-endosome interfaces may impair this dynamic remodeling process, thereby restricting organelle plasticity. To probe these dynamics, we employed a hypotonic swelling assay that induces the formation of large intracellular vesicles (LICVs), expanding organelle membranes and spatially separating compartments while preserving inter-organelle contacts. This reorganization enables real-time visualization of membrane remodeling and contact-site dynamics that are otherwise unresolved in intact cells[61].

SH-SY5Y cells and DNeurons were stained with MitoTracker Red CMXRos to visualize intact mitochondria. Under isotonic conditions, mitochondria in both control and αS-conditioned cells displayed a typical branched tubular network (Fig. S2a), with a modest reduction in network complexity observed for αS_{100D}. Upon hypotonic treatment, these networks rapidly fragmented into numerous mitochondrial LICVs over 30 min, reflecting normal remodeling between mitochondria (Fig. 2a and MovieS1). This assay thus provides a sensitive readout for contact-site flexibility and mitochondrial fission-fusion dynamics. The extent and kinetics of mitochondrial fragmentation and LICV formation reflect the capacity for membrane remodeling at ER-mitochondria interfaces. We next examined how the presence of spreading αS affects this process. DNeurons and SH-SY5Y cells were pre-exposed to αS for 14 h before undergoing hypotonic swelling, and organelle remodeling was monitored by time-lapse imaging (Fig. 2a and MovieS2 (αS), MovieS3 (αS_D)). Under hypotonic conditions, control cells showed extensive vesiculation. In contrast, αS-treated cells retained elongated mitochondrial structures. Quantitative segmentation of these images at the end of hypotonic treatment (30 min), revealed that the presence of αS markedly reduced LICV number while preserving elongated mitochondria (Fig. 2b-e). Mitochondria showed a dose-dependent decrease in LICV number following αS exposure (Fig. 2b, c), accompanied by increased mitochondrial branch length (Fig. 2d) and aspect ratio, a measure of length-to-width proportion (Fig. 2e). These concentration-dependent phenotypic differences were comparable between SH-SY5Y and DNeurons (Fig. S2b-d). Similar to full-length αS_D, αS_{100D} reduced mitochondrial LICV number; however, mitochondrial morphology, including branch length and aspect ratio, remained comparable to that of untreated controls (Fig. 2c-e, S2b-e, and MovieS4 (αS_{100D})). These findings indicate that αS restricts mitochondrial fragmentation and reshaping in response to cellular stress, consistent with impaired fission-fusion activity at these organelle contact zones.

Finally, to distinguish whether these effects arise from extracellular spreading αS or increased intracellular αS abundance, SH-SY5Y cells overexpressing αS-SNAP were analyzed. Although total αS levels were increased several-fold relative to cells treated with spreading αS (Fig. S2f), overexpression alone did not affect LICV formation, mitochondrial branch length, or aspect ratio (Fig. 2f-i and S2g). In contrast, when

cells expressing αS-SNAP that were also conditioned with extracellular αS, this recapitulated the characteristic phenotypes resulting in reduced vesiculation, and elongated mitochondria (Fig. 2f-i). These data demonstrate that specifically spreading αS recruited to inter-organelle contacts, rather than intracellular αS accumulation, disrupts the dynamic remodeling of MAM-endosome interfaces and constrains mitochondrial fission-fusion behavior. Together, these results indicate that αS accumulation at contact sites limits organelle membrane plasticity, likely by stabilizing otherwise transient MAM-endosome junctions.

Spreading αS reprograms mitochondria into a contact site-enriched, quality control-deficient state

Having established that spreading αS localizes to mitochondria-ER-endolysosomal contact sites, remodels MAM architecture, and constrains mitochondrial dynamics, we next sought to define the molecular machinery selectively associated with αS-engaged mitochondria. We reasoned that identifying this protein environment would elucidate the interorganelle pathways most directly perturbed by αS and provide mechanistic insight into downstream functional consequences. To this end, we performed quantitative LC–MS/MS-based proteomics on mitochondria isolated from control and αS_D-conditioned cells. Mitochondria were FAOS-sorted based on MitoTracker and internalized αS_{A647} signal. This approach yielded three distinct populations: control mitochondria (ctrl) from untreated cells, mitochondria co-sorted with internalized αS (αS^+ mitochondria), and mitochondria from αS-treated cells lacking detectable αS signal (αS^- mitochondria, Fig. 3a). Importantly, αS^- mitochondria represent an internal matched control derived from the same αS-exposed cells as αS^+. This strategy enabled discrimination between the global effects of αS exposure and protein networks specifically associated with αS-engaged mitochondrial populations. Quantitative mass spectrometry revealed that αS^+ mitochondria exhibited a proteomic profile that was clearly distinct from both ctrl and αS^- fractions. Principal component analysis demonstrated robust segregation of αS^+ mitochondria, while αS^- mitochondria clustered closely with ctrl samples (Fig. 3a). This suggested that proteomic remodeling induced by spreading αS is spatially restricted rather than uniform across the mitochondrial network. Differential expression analysis supported this observation. Comparison of αS^+ mitochondria to ctrl identified significant proteomic changes (2528 over-represented, 1240 under-represented proteins), which were similarly evident when comparing αS^+ to αS^- mitochondria (2601 over-represented, 1180 under-represented proteins). In contrast, αS^- mitochondria showed no significant proteomic changes relative to control (Fig. 3b and S3a).

To define pathways associated with αS-engaged mitochondria, we performed enrichment analysis across the sorted mitochondrial populations. Comparison of combined mitochondrial fractions from αS-treated cells ($\alpha S^+ + \alpha S^-$) against ctrl primarily captured global responses to αS exposure. Pathways associated with mitochondria contact sites, mitochondrial organization, lipid metabolism, and calcium signaling were enriched, consistent with activation of inter-organelle communication networks (Fig. S3b). In contrast, endolysosomal membrane organization and degradative trafficking pathways were depleted. Over-representation analysis (ORA) further confirmed the coherence of these pathways, revealing strong concordance in pathway enrichments between αS^+ vs ctrl and αS^+ vs αS^- comparisons (Fig. 3c and Fig. S3c). The connectivity network (cnet) representation further organized these pathways into two functionally distinct modules with no leading-edge protein overlap (Fig. 3d). A positively enriched module comprised pathways associated with mitochondrial bioenergetics, membrane architecture, ER–mitochondria contact sites, and mitophagy-related signaling. In contrast, a negatively enriched module contained pathways linked to autophagy execution, vesicle-mediated trafficking, and degradative cargo processing. This organization suggests a functional separation between pathways associated with contact-site engagement and upstream MQC signaling and those required for downstream execution and degradation. Heatmap analysis of

leading-edge proteins further supported this functional segregation at the level of individual proteins (Fig. 3e and S3d).

αS^{+} mitochondria were enriched in proteins associated with mitochondrial bioenergetics, membrane organization, and metabolic remodeling (Fig. 3f, Fig. S3e and Supplementary Table 1). These included multiple components of the electron transport chain, such as NDUFS subunits, the Complex III subunit UQCRQ, and the respiratory supercomplex assembly factor COX7A2L, as well as regulators of mitochondrial structure, including OPA1 and TOMM family translocase subunits. Proteins associated with ER–mitochondria tethering and calcium exchange were coordinately enriched, including the MAM-associated tethers VAPB and RMDN3, MFN1/2, VDAC1/2/3, and ITPR1/2, together with components of the MCU, MICU1, MICU2, and LETM. ER-localized MAM proteins, including CANX, BCAP31, and the ER stress kinase EIF2AK3/PERK, were also enriched, supporting activation of ER–mitochondria stress signaling pathways. In parallel, enzymes linked to cardiolipin biosynthesis and membrane remodeling, including CRLS1, DNAJC19, and PNPLA8, were elevated, consistent with reorganization of mitochondrial membrane composition at contact interfaces.

Conversely, proteins associated with downstream mitochondrial turnover and degradative trafficking were coordinately depleted (Fig. 3f, Fig. S3e and Supplementary Table 1). Components of ubiquitin-mediated cargo tagging, including multiple E1/E2/E3 enzymes, were reduced alongside core autophagy machinery (ATG7/12, and ATG13/101) and selective autophagy receptors, including SQSTM1/p62, OPTN, and TAX1BP1. Proteins involved in mitochondrial transport, including kinesin motor subunits (KIF1A and KLC family members), were similarly depleted. In parallel, machinery required for membrane scission, endosomal sorting, and cargo resolution, including CHMP and VPS37 family proteins, PDCD6IP/ALIX, BLOC-1complex subunits, AP-3 adaptor components, and the mitophagy regulator TBC1D15, was reduced, consistent with impaired downstream trafficking and turnover capacity. Notably, endogenous SNCA was also reduced in αS-associated mitochondrial fractions, suggesting redistribution of the native αS pool. Several protein pairs further suggested a selective enrichment of membrane-engagement and docking machinery and the depletion of proteins required for downstream remodeling and trafficking. The mitochondrial fission receptor MFF was enriched, while its effector GTPase DNM1L/DRP1was reduced, consistent with impaired mitochondrial fragmentation in αS-associated mitochondria. Similarly, the trafficking adaptors RHOT1 and RHOT2 were enriched, while kinesin motor proteins were depleted, suggesting preserved mitochondrial docking but reduced transport capacity. Although αS^{-} mitochondria showed no significant protein changes relative to control, ORA identified weak but coordinated pathway-level shifts within this fraction (Fig. S3f). These were primarily linked to RNA-related and mitochondrial stress-response pathways, including mt-tRNA processing, iron–sulfur cluster assembly, and electron transport chain regulation[62]. In contrast, P-body assembly pathways were relatively depleted[63]. Thus, while the major proteomic remodeling was restricted to αS-associated mitochondria, αS exposure also induced lower-magnitude secondary responses. Together, these data suggest that αS engagement promotes an interorganelle contact site-enriched mitochondrial state with reduced association of downstream degradative machinery.

Spreading αS at tri-organelle contact sites impairs neuron-to-astrocyte mitochondria transfer

The proteomic enrichment of vesicular trafficking and MQC pathways within αS-associated mitochondrial fractions suggested that αS engagement at contact sites may extend beyond intracellular remodeling to affect pathways governing mitochondrial turnover and intercellular exchange. Mitochondria are

increasingly recognized as transferable organelles, exchanged between neurons and glial cells to support stress adaptation and metabolism[41] . Importantly, mitochondrial fission, endolysosomal trafficking, and ER-mitochondria contacts play key roles in coordinating mitochondrial export and uptake[32–34,57,58]. We next asked whether spreading αS alters neuron–astrocyte mitochondrial transfer.

We examined mitochondrial exchange between iPSC-derived DNeurons and hiPSC-derived astrocytes (hAstrocytes) or human astrocytoma cells (CCF-STTG1, CCFs) using a non-contact co-culture system that permits intercellular transfer of organelle-derived vesicles without direct cell-cell contact (Fig. 4a). Mitochondria were differentially labeled in neurons and astrocytes, enabling quantitative assessment of bidirectional mitochondrial transfer under basal and stress-induced conditions. Neuronal mitochondria were labeled with MitoTracker Green FM and astrocytic mitochondria with MitoTracker Red CMXRos. Under basal conditions, neuronal mitochondria were detected within astrocytes after 14 h of co-culture, indicating spontaneous transfer (Fig. S4a). This was quantified by the neuronal mitochondrial fluorescence signal in astrocytes (Fig. S4b). Transfer efficiency further increased following oxidative stress induced by hydrogen peroxide (H_2O_2, Fig. 4b, c). Transferred neuronal mitochondria appeared as discrete puncta within recipient cells and localized to Lamp1-positive lysosomes (Fig. S4c), suggesting delivery for degradation. Conversely, astrocyte-derived mitochondria detected in neurons integrated into the neuronal mitochondrial network (Fig. S4d), supporting functional incorporation[41,64].

Strikingly, conditioning neurons with spreading αS markedly impaired this process. In the presence of αS localized to tri-organelle MAM-endosome sites, the transfer of neuronal mitochondria to hAstrocytes and CCFs were reduced by nearly twofold, even under H_2O_2 stress (Fig. 4c, d). The extent of this impairment scaled with αS concentration (Fig. 4e and Fig. S4e). This αS-dependent impairment of mitochondrial transfer is also evident under non-stress-induced conditions (Fig. S4b). Correspondingly, astrocytes co-cultured with αS-conditioned neurons exhibited a decrease in endo/lysosomal pool containing neuronal mitochondria (Fig. 4f, g), measured by immunostainings for Lamp1 and Rab5. This indicates reduced neuronal mitochondrial uptake and degradation by astrocytes. In parallel, quantification of neuronal mitochondrial DNA (mtDNA) using PicoGreen staining confirmed a significant reduction of neuronal mtDNA signal within astrocytes upon αS spreading (Fig. 4h). Interestingly, the reciprocal transfer of astrocytic mitochondria to neurons was enhanced (Fig. 4i). However, the neuronal mitochondria remained elevated compared to control where efficient transfer occurred (Fig. 4j). This bidirectional imbalance suggests that αS selectively interferes with the export of damaged neuronal mitochondria while maintaining or even promoting compensatory import of astrocytic mitochondria.

In a similar setup, αS_{100D} did not affect mitochondrial transfer from neurons to astrocytes (Fig. 4c, k, and Fig. S4f). These results indicate that the C-terminus of αS, and its associated disruption of calcium homeostasis[42,65], is required for regulating mitochondrial export in neurons. Collectively, these findings reveal that spreading αS interferes with the normal directional exchange of mitochondria between neurons and astrocytes (Fig. 4c, k). We propose a twofold mechanism: (i) αS accumulation at MAM-endosome contact sites impairs mitochondrial fission and prevents damaged neuronal mitochondria from being transferred to astrocytes for degradation, and (ii) excess import of astrocytic mitochondria into neurons perturbs the stoichiometric balance of mitochondrial turnover and calcium buffering. Together, these effects may contribute to the progressive metabolic imbalance and neuronal vulnerability observed during the early stages of αS spreading and propagation in synucleinopathies.

Discussion

The present study identifies organelle contact sites as an early and previously unrecognized target of spreading αS. Incoming monomeric αS preferentially localizes to mitochondria-ER-endolysosomal interfaces, where it remodels organelle communication and compromises MQC pathways. These findings suggest that recipient-cell responses to extracellular αS begin at discrete regulatory hubs that coordinate organelle dynamics and homeostasis, providing a mechanistic link between αS spreading and mitochondrial dysfunction in synucleinopathies.

A major implication of our findings is that extracellular αS does not distribute uniformly within recipient cells but instead accumulates at specialized contact-site populations. Organelle contact sites are increasingly recognized as signaling platforms[60] that integrate endolysosomal sorting[66], calcium homeostasis[31], mitochondrial dynamics[32,34], and stress responses[36,67]. The preferential recruitment of αS to tri-organelle interfaces therefore suggests that these structures represent vulnerable nodes through which relatively small amounts of transferred αS can exert disproportionate effects on cellular organization. Since αS used in this study is monomeric and below concentrations associated with aggregation[68], our findings support a model in which contact-site dysfunction precedes the formation of classical αS pathology and may contribute to the earliest stages of disease progression.

Our data further suggest that the primary consequence of αS accumulation at contact sites is a loss of organelle plasticity. Dynamic remodeling of ER–mitochondria and endolysosomal contacts[61] is essential for mitochondrial fission[32,34], trafficking[58,66], and quality control. We propose that αS stabilizes normally transient interactions, increasing organelle connectivity while reducing the flexibility required for adaptive remodeling. Such stabilization could impede the segregation and processing of damaged mitochondria, resulting in altered contact-site architecture and impaired MQC. Taken together, our findings suggest that mitochondrial dysfunction emerges not from an immediate loss of mitochondrial activity but from a progressive inability to remodel and eliminate damaged organelles.

The proteomic organization of αS-associated mitochondria supports this interpretation. Rather than exhibiting signatures of generalized mitochondrial failure, αS-associated mitochondrial fractions were enriched in pathways linked to organelle tethering, membrane remodeling, and metabolic regulation while displaying reduced representation of degradative trafficking and autophagic machinery. This pattern suggests a functional uncoupling between mitochondrial engagement and mitochondrial turnover. Mitochondria remain integrated within organelle communication networks yet become less efficiently connected to pathways responsible for their clearance. We therefore propose that spreading αS promotes a contact site-enriched but quality control-deficient mitochondrial state, characterized by persistent organelle connectivity and reduced degradative capacity. Importantly, these changes were restricted to αS-engaged mitochondrial populations, indicating that spreading αS selectively remodels discrete mitochondria. More broadly, this organization may reflect a cellular response to incoming αS. Although not directly tested here, such a model could contribute to the persistence of both dysfunctional mitochondria and intracellular αS within recipient cells.

The disruption of neuron-astrocyte mitochondrial transfer extends the consequences of contact-site remodeling beyond cell-autonomous dysfunction. Intercellular mitochondrial exchange is increasingly recognized as an important mechanism through which neural cells maintain tissue-level homeostasis during stress[36–41]. By reducing the transfer of neuronal mitochondria to astrocytes while enhancing the reciprocal delivery of astrocytic mitochondria, spreading αS appears to shift this system from mitochondrial disposal towards compensatory support. Such a response may temporarily preserve neuronal function but would be expected to favor the accumulation of damaged mitochondria within neurons. These findings suggest that

defects in intercellular MQC may arise at early stages of αS spreading, before the emergence of neurodegeneration.

In summary, our findings support a model in which early αS spreading initiates mitochondrial dysfunction by altering the coordination of mitochondrial dynamics, quality control, and neuron–astrocyte communication. The spreading of αS shifts mitochondria toward a state of enhanced connectivity but impaired turnover. These events occur prior to aggregation and identify organelle contact sites as a potentially targetable vulnerability linking αS propagation to the earliest stages of synucleinopathies.

Limitations and future directions

Several questions remain to be addressed. First, while our proteomic analysis identifies candidate pathways and proteins associated with αS-engaged mitochondria, the precise molecular interactions mediating αS recruitment to contact sites remain to be defined. Determining whether αS directly binds specific tethering complexes or alters membrane properties will be critical for understanding its mechanism of action. Second, the extent to which these findings translate *in vivo* and contribute to disease progression remains to be investigated. In particular, assessing how αS-mediated disruption of mitochondrial transfer impacts neuronal survival and circuit function. Third, our mitochondrial sorting strategy enables enrichment of αS-associated mitochondrial fractions, but it also has technical limitations. Contact-site proteins may be partially lost or redistributed during lysis, FAOS, and sample preparation for MS. Thus, the proteomic data should be interpreted as defining αS-associated mitochondrial populations rather than purified contact-site structures. Fourth, the mitochondrial transfer assay models vesicle-mediated exchange in a non-contact co-culture system. This design isolates transfer of organelle-derived material without direct cell–cell contact, but it does not capture tunneling nanotube–dependent mitochondrial transfer or other contact-dependent mechanisms. Therefore, future studies should test whether αS similarly disrupts mitochondrial exchange in contact co-culture systems and in animal models. Finally, the interplay between monomeric and aggregated αS species at contact sites remains unclear. The bidirectional imbalance in mitochondrial transfer suggests that targeting intercellular MQC pathways could be a therapeutic strategy. Enhancing mitochondrial export or restoring contact-site dynamics may help re-establish cellular homeostasis in the presence of spreading αS.

Methods

Neuronal iPSC-derived cultures

The human iPSC line BIHi005-A was maintained in Essential 8 Flex medium (E8+; Thermo Fisher, #A2858501) on Geltrex-coated 6-well plates at 37 °C, 5% CO2 and 1% O2, and passaged at 70–80% confluency with 0.5 mM EDTA (1:6 split). Neural progenitor cells (NPCs) were generated using the monolayer protocol of the STEMdiff Neural Induction Kit (STEMCELL, #A1647801; NIM+). iPSCs were dissociated with Accutase, seeded onto Geltrex in E8+ with 5 μM ROCK inhibitor (1×10^6 cells per well). At ~90% confluency, differentiation to NPCs was induced by daily medium change with NIM+. After one week, cells were passed through a 100 μm strainer and reseeded in NIM+ (1.5×10^6 cells per well). NPCs were maintained at 37 °C, 5% CO2 and 1% O2, with daily medium changes, and passaged at 70–80% confluency every 2–3 days for 8–9 passages. For midbrain DNeuron differentiation, NPCs were seeded onto poly-L-ornithine (PLO)/laminin-coated plates (1.2×10^6 cells per well) in NEM+, then differentiated for 6 days with daily medium changes using the STEMdiff Midbrain Neuron Differentiation Kit (STEMCELL, #10-0038). Neurons were then dissociated with Accutase, reseeded onto PLO/laminin (7×10^4 cells/cm) in STEMdiff Midbrain Neuron Maturation Medium (STEMCELL, #100-0041), and

matured for 14 days with half-medium changes every 2–3 days. Neuronal identity and functional maturation were confirmed by immunofluorescence and calcium imaging[69].

iPSC-derived human astrocyte differentiation

Human iPSC-derived astrocytes were generated from BIHi005-A NPCs as described[70,71] with minor modifications. After a minimum of 4 NPC passages, NPCs were detached with Accutase, passed through a 100 µm strainer and plated at 5×10^5 cells per well on Geltrex-coated 6-well plates. The following day, medium was exchanged for astrocyte differentiation medium (DMEM with 2 mM GlutaMAX-I, 1% N-2, 1% FBS, 20 ng/ml CNTF (Miltenyi Biotec) and 1% penicillin/streptomycin), refreshed every 2–3 days. At 80–90% confluency, cells were subcultured 1:2–1:3 onto fresh Geltrex. Differentiation continued for up to 6 weeks until proliferation ceased, after which cells were maintained at high density and passaged weekly. Astrocyte identity was confirmed by GFAP and S100β immunofluorescence.

Co-culture assays to monitor mitochondrial transfer

Non-contact co-cultures were assembled in 24-well plates using three paraffin wax pillars per well as spacers. Neurons were seeded on PLO/laminin-coated wells and astrocytes on Geltrex-coated 12 mm coverslips. αS-treated (14 h) and untreated DNeurons were labelled with 100 nM MitoTracker Green FM (Thermo Fisher, #M7514) or PicoGreen (1:1000; Thermo Fisher Scientific P11496); immortalized and hiPSC-derived astrocytes were labelled with 50 nM MitoTracker Red CMXRos (Thermo Fisher, #M7512), cells were washed twice with warm dPBS. Where indicated, neurons were treated with 50 µM H_2O_2 for 8 h after labelling to induce oxidative insult. Astrocyte coverslips were then inverted onto the paraffin pillars of neuron-containing wells and topped up with fresh maturation medium, and co-cultures were incubated for 15 h (37 °C, 5% CO2). For imaging, the medium was replaced with BrainPhys Imaging Optimized Medium (STEMCELL, #05796). The astrocytic compartment was fixed and stained for Lamp1 and Rab5 to assess the endolysosomal pool. Imaging was performed on a Dragonfly spinning-disk confocal microscope (Andor, Oxford Instruments) or a PicoQuant MicroTime 200 time-resolved fluorescence system. Mitochondrial transfer was quantified in two designs: (1) bidirectional transfer between MitoTracker-labelled neurons and astrocytes, and (2) uptake of neuronal mtDNA by MitoTracker-labelled astrocytes using PicoGreen-labelled neurons.

Cell culture

SH-SY5Y (RRID: CVCL_0019) and CCF-STTG1 (RRID: CVCL_1118) cells (ATCC) were cultured at 37 °C, 5% CO_2 in DMEM or RPMI, respectively, supplemented with 10% FBS, penicillin and streptomycin. Cells passaged at ~95% confluence with 0.05% trypsin-EDTA (Life Technologies).

For imaging, SH-SY5Y cells were seeded in eight-well Ibidi chambers (4×10^4 cells/well) for 48 h, then treated with ATTO700-/Alexa647-labelled αS at 80 nM (αS) or 250 nM (αS_D/αS_{100D}) for 14 h. Medium exchanged followed a 10 min recovery before imaging.

αS purification

αS was expressed in E. coli BL21 cells; for αS, BL21 stocks containing the N-terminal acetyltransferase B (NatB) plasmid with orthogonal antibiotic resistance were used. αS constructs were expressed at OD600 ≈ 0.4-0.5 by induction with 320 µM IPTG (2 h, 37 °C). Cells were pelleted and resuspended in fresh lysis buffer (25 ml per 0.5 l; 40 mM NaOH, 20 mM Tris pH 8.0, 1 mM EDTA, 1mM PMSF, 0.1% Triton X-100), supplemented with 1 mM PMSF and protease inhibitor. The purification of αS full length protein and αS_{100} was carried out as previously described[72,73], with minor modifications. Briefly, two

ammonium sulfate cuts were used (0.116 g/mL and 0.244 g/mL) with αS precipitating in the second step. The pellet was resolubilized and dialyzed to remove ammonium sulfate overnight. Dialyzed samples were filtered through a 0.22 µm filter, loaded to an anion exchange column (GE HiTrap Q HP, 5 ml) and eluted with a gradient to 1 M NaCl. αS eluted at approximately 300 mM NaCl. Fractions containing αS were pooled, concentrated using Amicon Ultra concentrators and buffer exchanged. Concentrated samples were then loaded to a size exclusion column (GE HiLoad 16/600 Superdex75) and eluted at 0.5 ml/minute. Fractions containing αS were confirmed by running an SDS-gel, concentrated and processed for labeling.

αS labeling

For site-specific labeling of αS, a cysteine was introduced at residue 9 (S9C point mutation). Purified αS was incubated with 1 mM dithiothreitol (DTT) for 30 min at RT to reduce cysteines. Buffer exchange was performed into 6 M guanidine hydrochloride (GdmCl) buffer using Amicon Ultra concentrators. The protein was incubated with 4-fold molar excess ATTO700 or Alexa647 maleimide (Invitrogen) (overnight, 4 °C) under stirring conditions. Following buffer exchanged using Amicon Ultra concentrators, excess dye and GdmCl was removed by passing the solution through two coupled HiTrap Desalting Columns (GE Life Sciences, Pittsburgh, PA). Fractions containing labeled αS were pooled, diluted to ~30 µM, snap-frozen and stored at -80 °C. Concentration and momomeric state of labelled protein was verified using fluorescence correlation spectroscopy on a PicoQuant MicroTime 200 time-resolved fluorescence system to check for degradation or aggregation. Alexa647-labeled αS was utilized for FAOS and MS/proteomic studies, all other experiments were performed with ATTO700-labeled αS.

Transfection and nucleofection

At ~80% confluency, SH-SY5Y cells were transfected with SPLICS Mt-ER short P2A (addgene #164108) using Lipofectamine 3000 (Invitrogen #L3000001; following manufacturer's instructions), with 250 ng plasmid DNA per well for 30-36 h.

Stable overexpression cell lines were generated by nucleofections of SH-SY5Y cells using the Amaxa SF Cell Line 4D-Nucleofector Kit (Lonza #V4XC-2024; following manufacturer's instructions), with 250 ng of plasmid: αS-SNAP plasmid was generated (pCMV-αS-SNAP, SNAP-tag C-terminal), mCherry-VAPB purchased from addgene (#108126). Cells were selected by treatment with 300 µg/ml geneticin, expression was verified with fluorescence imaging.

Hypotonic Cell Treatment

To generate large intracellular vesicles (LICVs) from mitochondria, SH-SY5Y cells conditioned with and without αS were treated with hypotonic media (10% DMEM in water, pH ~ 7), incubated at 37 °C with 5% CO2 for 10 min to allow for Mito-LICV generation, and then imaged as previously shown[61]. DNeurons were treated with hypotonic LICV media (50% DMEM in water, pH ~ 7), incubated at 37 °C with 5% CO2 for 10 min to allow for mito-LICV generation, before image acquisition. Following hypotonic treatment, cells remained stable in the imaging chamber for approximately 30-60 min. Following longer exposure to hypotonic solution, cells disintegrate, burst and/or detach from the dish. Pre-maturely detached or lysed cells were not imaged or utilized in this study.

Live cell fluorescent organelle dyes and stains

Cells were treated with 20 nM MitoTracker Red CMXRos (Thermofisher, #M7512) for 30 mins before imaging. For mitochondrial transfer assays, neurons were treated with 100 nM MitoTracker Green FM (Thermofisher, #M7514), astrocytes with 50 nM MitoTracker Red CMXRos for 30 min prior to H_2O_2

518 treatment and co-culturing. mtDNA was labelled in neurons using PicoGreen dsDNA reagent (Quant-iT™,
519 P11496, Thermo Fisher Scientific) at a 1:1000 dilution from the concentrated stock solution. For
520 colocalization of αS and endolysosomes, cells were treated with 400 nM LysoSensor Green DND-189
521 (Thermofisher, #L7535) for 30 mins before imaging. Cells imaged on the ANDOR Dragonfly system were
522 stained with 2 µg/ml Hoechst for 5 min. Prior to imaging, samples were changed into fresh imaging media
523 and incubated for ~10 min.
524
525 **Immunofluorescence**
526 Cells were fixed for 15 min with 4% PFA (w/v) (SH-SY5Y) or 4% PFA and 4% sucrose (DNeurons and
527 astrocytes), supplemented with 0.1% glutaraldehyde. Cells were washed 3x with dPBS after fixation and
528 every subsequent step. Cells were permeabilized (0.2% Triton X-100 in dPBS, 5 min), then blocked
529 (0.5% BSA, 10% normal goat/donkey serum; 1h at RT). Primary staining was performed (3% BSA,
530 overnight at 4 °C), using primary antibodies as follows: for endolysosomal pool characterization, anti-Rab5
531 (rabbit, abcam #ab218624; at 1:200) and anti-LAMP1 (mouse, DSHB #AB_2296838, at 1:200); for QC of
532 DNeurons, anti-TH (rabbit, Abcam #ab152; at 1:200), anti-FoxA2 (goat, R&D Systems #AF2400; at
533 1:100), anti-Tubulin-β3 (mouse, Biolegend #801201; at 1:500); for QC of iPSC derived h-astrocytes, anti-
534 GFAP (rabbit, Agilent #Z033429-2; at 1:200), anti-S100β (rabbit, abcam #ab52642; at 1:100).Cells were
535 washed and secondary antibody staining was performed (0.5% BSA, 1-2 h at RT, all at 1:800-1000) with
536 secondaries: anti-rabbit Alexa647 (abcam #ab150075), anti-mouse Alexa488 (Life Technologies
537 #A21202); anti-rabbit Alexa594 (Life Technologies #A11012); anti-goat Alexa680 (Invitrogen #A21084).
538 During the last wash DAPI was added at 0.4 µg/ml.
539
540 **Cell imaging**
541 Live cell imaging was performed at 37 °C and 5% CO_2. For hypotonic cell swelling assays in DNeurons,
542 and for quantitative analysis of mitochondrial transfer, live cell samples were imaged on an ANDOR
543 Dragonfly spinning disk confocal microscope (Andor, Oxford Instruments, Abingdon, UK) equipped with
544 a 63 × Plan-Apo/1.1-NA glycerol-immersion objective. Across conditions within the same experimental
545 replicate, excitation/emission (ex./em.) and gain settings for the channels were kept constant: DAPI,
546 Hoechst - 405/450; MitoTracker Green FM, SPLICS – 488/525; mCherry, MitoTracker Red CMXRos –
547 561/600; ATTO700-αS, Alexa647-αS – 637/700.
548 All other imaging was carried out on a PicoQuant time-resolved fluorescence system with a TCSPC
549 MicroTime 200 module, based on an inverted Olympus IX73 microscope (Olympus, Tokyo, Japan) with a
550 60X Plan-Apo/1.4-NA water-immersion objective and 479/560/680 nm excitation lasers. Time-gated
551 pulsed interleaved excitation (PIE at 26.76 MHz) was conducted throughout all acquisitions, with a triple-
552 line beamsplitter directing signals to SPAD detectors. Images were acquired at a frame size of 428 × 428
553 pixels and a dwell time of 150 µs, resulting in a frame-acquisition speed of 55 s. For time-lapse imaging,
554 these settings were maintained continuously for 30 min, interrupted only by re-adjusting the z-plane if
555 necessary. Images acquired with this instrument were in fluorescence lifetime mode but integrated in the
556 SymPhoTime 64 software (PicoQuant, Berlin, Germany) to obtain intensity-based images.
557
558 **Western blots**
559 For protein extraction, cultured cells were scrapped off and lysed with RIPA buffer, with 1x Protease
560 Inhibitor Cocktail (Sigma Aldrich) for 45 min on ice, vortexing every 5 min and sonicating 3x for 1 min in
561 a water bath sonicator. To remove cell debris the solution was centrifuged for 20 min at 10,000 rpm at 4 °C.
562 Protein concentration was calculated using the BCA Protein Assay Kit (Thermofisher). Protein samples (40

and 20 µg) were mixed with 4x Laemmli Buffer and boiled at 95 °C for 5 min. Samples were loaded on 8 – 16 % Tris-Glycine Plus WedgeWell precasted gels (Invitrogen), separated by SDS-PAGE and transferred to 0.45 µm PVDF membranes (Sigma Aldrich). Membranes were blocked for 2 h at room temperature with 5% BSA in 1x TBST and incubated overnight at 4 °C, with primary antibodies diluted in the same solution against αS (rabbit anti-alpha + beta Syn, 1:1000, ab51252, Abcam) and vinculin (mouse anti-vinculin, 1:1000, V9131, Sigma Aldrich). Membranes were washed, incubated for 1 h with the appropriate secondary antibody conjugated to horseradish peroxidase (Cell Signaling) at room temperature, and the immunoblots were developed using ECL Western Blotting Detection Reagent (Cytiva). The Gelanalyzer Software was used for imaging and analysis.

Sample preparation for FAOS sorting

Cells were treated with Alexa647-labelled αS or αS_D, 14h prior to the experiment. Cells were harvested, pelleted, then lysed with custom-made mild lysis buffer (10 mM Tris-HCl, 10 mM NaCl, 3 mM $MgCl_2$, 0.01% NP-40, 1 mM DDT, 1x protein inhibitor cocktail +EDTA, 1 µM PMSF, in nuclease-free H_2O). Samples were kept on ice for 10 min, resuspending every 2 min, then sonicated (one cycle, 5 s) in a sonicator bath. Lysates were filtered through 30 µm strainers, rinsing strainers once with washing buffer (dPBS, 1x protein inhibitor cocktail + EDTA, 1µm PMSF). Lysates were incubated on ice for 5 min prior to staining with 100 nM MitoTracker Green FM (Invitrogen M7514) for 10 min on ice. Lysates were filtered through a 20 µm strainer into Polypropylen FACS tubes and subjected to FAOS.

Fluorescence-Activated Organelle Sorting (FAOS)

Whole-cell lysates were sorted on a BD FACSDiscover S8 cell sorter (BD Biosciences) equipped with BD CellView Image Technology and BD SpectralFX Technology, operated via FACSChorus software (v6.2). From the standard five-laser configuration and three imaging detection channels, MitoTracker Green FM was excited by the 488 nm laser, detected spectrally and imaged on the CellView imaging detector, αS_{A647} was excited by the 637 nm laser. Spectral unmixing was performed using the FACSChorus unmixing algorithm with single-stained or unstained controls. Sorting was performed (4 °C, 400 rpm) with the 85 µm nozzle configuration (35 psi, 57 kHz) in Purity mode at a FACSChorus flow rate setting of 10–20, adjusted according to sample concentration. A four-gate hierarchy (P1–P4) was applied to isolate individual mitochondrial entities on the basis of MitoTracker Green fluorescence, axial light loss, and BD CellView imaging features (eccentricity, radial moment, and centre of mass), followed by separation into αS_{A647}-positive (αS^+) and -negative (αS^-) mitochondrial populations. Mitochondrial events (P1) were identified by MitoTracker Green FM fluorescence in combination with BD CellView imaging, selecting morphologically small, circular structures by axial light loss and imaging parameters. Singlet events were isolated from P1 (P2) by exclusion of elongated and aggregated events based on eccentricity and radial moment. Centered events (P3) were selected from P2 by center-of-mass gating to retain only events fully contained within the imaging field of view. From P3, αS-associated (αS^+) and αS-negative (αS^-) mitochondrial populations were resolved spectrally by A647 fluorescence (P4).

Sorting was continued until the entire lysate volume was processed rather than to a fixed event target, to maximize recovery of αS-associated mitochondrial events. Across samples, 107,000–190,000 αS^- mitochondrial events and 2,500–5,500 αS^+ events were collected from αS-treated samples, and 100,000–120,000 total mitochondrial events from control samples. Variation in total event counts reflected differences in sample loss during filtration and lysis efficiency. Samples were collected simultaneously into 1.5 mL LowBind Ependorf tubes pre-filled with washing buffer, maintained at 4 °C during sorting and

flash-frozen immediately after. Data were exported in FCS 3.2 format and analyzed in FlowJo (v.10) with the BD CellView Lens Plugin for concurrent analysis of imaging and spectral parameters.

Sample processing and Mass Spectrometry

For each sample with 3000 mitochondrial events or less, the whole sample was taken for subsequent processing. Otherwise, a fraction of the sample, equivalent to 3000 mitochondrial events, was used to ensure that all subsequent steps were performed on the same amount of starting material. The samples were spun down (18,000 x g) for 15 min at 4°C and the supernatant removed. 15 µl of 0.1% N-Dodecyl-β-D-maltoside was added in the presence of 100 mM triethylammonium bicarbonate buffer, 5 mM tris(2-carboxyethyl)phosphine) and 20 mM chloroacetamide. Mitochondria were lysed by sonication (10 min, 30 sec on 30 sec off at 4 °C) using a Bioruptor (Diagenode, Seraing, Belgium). Samples were incubated overnight with a mixture of Lys-C (20 ng) and trypsin (20 ng) at 37 °C. The digestion was quenched with formic acid and then cleaned using Evotip Pure C18 tips (EV2013, Evosep, Odense, Denmark). Tips were eluted with 35% ACN in 0.1% formic acid. Samples were dried and resuspended in 5.4 µl of loading buffer. 5 µl of the sample was injected.

Peptides were analyzed using a label-free data-independent acquisition (DIA) workflow on an Orbitrap Astral Mass Spectrometer (Thermo Fisher Scientific, Waltham, MA USA) coupled to a Vanquish Neo UHPLC system (Thermo Fisher Scientific) operating in nano-flow mode. Peptides were separated on a 75 µm x 20 cm analytical column (packed in-house with 1.9 µm C18 resin; Reprosil-Pur 120 C18-AQ, Dr. Maisch) applying a flow of 250 nl/min over 17.5 min using solvent A (0.1% FA, 3% ACN) and solvent B (0.1% FA in 90% ACN). Briefly, from 0 to 1 min solvent B was increased from 2 to 7%, followed by an increase to 20% and 30% solvent B, in 10 and 7.5 min, respectively. Solvent B was ramped up to 60% B over 2 min, followed by column washing at 90%B. Total run time was 25 min. The column was then equilibrated at high flow with a column equilibration factor of 3. For the DIA method, MS1 acquisitions were performed in the Orbitrap analyzer with a scan range from 380–1100 *m/z* at a resolution of 240,000, normalized Automatic Gain Control (AGC) of 500% and a maximum injection time of 5 ms. MS2 acquisitions were performed using a range from 400-800 *m/z*, an isolation width of 4 Th, a maximum injection time of 8 ms, a normalized AGC of 500% at 25% collision energy.

Proteomic data analysis and representation

Raw data were processed in Spectronaut 20[74] (Biognosys, build 20.2.250922.92449) against the reviewed *Homo sapiens* UniProt database (2023-05; 20,407 entries) using default settings, with cross-run normalization enabled and imputation disabled. Trypsin and endopeptidase Lys-C were specified as digestion enzymes. All downstream analyses were performed in R (v. 4.5.2; https://www.r-project.org/). For each comparison, proteins were retained if quantified in the relevant sample set (pairwise: αS^+ vs. control, αS^- vs. control; pooled: $\alpha S^+/\alpha S^-$ vs. control). Sample clustering was assessed by principal component analysis on log2-transformed protein intensities. Differential abundance between αS^+, αS^- and control was assessed using moderated t-tests (pairwise) in limma[75] (v. 3.66.0), with empirical Bayes moderation using an intensity-dependent mean–variance trend. P-values were adjusted by the Benjamini–Hochberg procedure; proteins were considered differentially abundant at FDR < 0.05 and |log2 fold-change| > 1. Gene symbols were mapped to Entrez IDs using biomaRt[76] (v. 2.66.0). Gene set enrichment analysis (GSEA) was performed on individual and pooled comparisons using clusterProfiler[77] (v. 4.18.1) against Gene Ontology (GO), Reactome and KEGG term sets. Differentially expressed proteins (DEP) were filtered by eulerr package (v. 7.0.4; https://doi.org/10.32614/CRAN.package.eulerr) for shared, as well as unique DEPs within αS^+ vs. ctrl and αS^+ vs. αS^- comparisons. Then both shared and unique DEPs were

subjected to over-representation analysis (ORA). Terms appearing in both comparisons' unique lists with non-overlapping gene fingerprints were excluded. For both GSEA and ORA, enrichment outputs were filtered to a custom curated list of existing mitochondria- and organelle-related terms in databases across GO, Reactome, KEGG and MitoCarta[78]. Redundancy of GO, Reactome Pathway and KEGG terms was reduced by semantic similarity and hierarchical relationships, and representative parent terms were selected, summarizing related biological child-terms. For Cnet and heatmaps, pairwise Jaccard similarity of leading-edge protein sets (threshold 0.60) was performed. Retained terms were filtered manually and visualized as dot plots, or Cnet and heatmaps using ggplot2 (v. 4.0.0), igraph (v. 2.2.1) and pheatmap (v. 1.0.13).
In parallel, a curated list of 207 proteins of interest (177 detected in this dataset) across 13 functional categories (Supplementary Table S1) was compiled from literature. DEPs were visualized as volcano plots using ggplot2, with proteins of interest color-coded by manually defined functional categories over a background of all detected proteins.

Data analysis

Chromatic aberration correction. To correct for chromatic aberration between fluorescence detection channels on the PicoQuant System, image registration was performed using a custom Python-based pipeline. Registration was performed using the SimpleITK library[79] (version 2.4.1), employing a translation transform optimized by the Mattes Mutual Information metric computed over 500 histogram bins, thereby enabling calibration-free image registration. Optimization was performed using a Regular Step Gradient Descent optimizer with a learning rate of 1.0, a minimum step size of 1×10^{-5}, a maximum of 1,000 iterations, and a gradient magnitude tolerance of 1×10^{-8}. During optimization, B-spline interpolation was applied to the moving image; the final registered channel was resampled onto the fixed image grid using linear interpolation.
For each three-channel image, channel 1 served as the fixed reference, to which channels 2 and 3 were independently registered. Pixel-size information lost during registration was recovered from the original images. Colocalization analysis was restricted to object-based approaches.

Fluorescence intensity line profiles. Line segments (6-10 µm) were manually drawn across in Fiji and line-intensity values for each channel were extracted (Fiji's plot profile function). Profiles from multiple regions (n = 2-3) were stacked and plotted using a custom Python script. Channel intensities were normalized using scaling factors to visualize spatial relationships.

Segmentations. Cell-area segmentations were either performed using Cellpose[80,81] (v3.1.1.) or in Fiji. Neuronal soma were segmented using the built-in cyto3 model with automatic diameter estimation, and predicted masks were manually curated in the Cellpose GUI to correct segmentation errors. In Fiji, saturation-threshold images were generated, converted to binary masks and built-in binary operations were applied for refinement using the same combination across all images from the same experiment. Masks of cell soma were used to calculate per-cell area or combined for per-image cell area. Mitochondria were segmented manually in Cellpose by tracing each mitochondrial object in the Cellpose GUI annotation interface; automated prediction was not used to delineate partially or fully fragmented mitochondrial networks accurately.

MAM measurements. MAM and αS puncta were detected using the radial symmetry-based spot detection algorithm RS-FISH[82] (Fiji Plugin). To obtain puncta areas for size quantification, detected coordinates were expanded into circular ROIs using a custom-built Fiji macro that performs full-width-at-half-maximum

(FWHM)-based radial profiling with adaptive thresholding. Size limits of 0.15–0.70 µm radius were applied for MAM puncta and 0.20-80 µm based on manually measured size ranges. Puncta exhibiting anisotropic expansion profiles (max./min. radius ratio >2.5) were flagged and excluded from size analysis. Measurements displaying artifactual clustering at size-limit cutoffs (9.8% of data) were removed prior to statistical analysis and plotting.

MAM density was calculated as the number of RS-FISH-detected puncta per cell area, expressed as puncta per 1000 µm². MAM size (radius [µm] and area [μm^2]) was quantified from FWHM-expanded ROIs. Statistical comparisons were performed using linear mixed models (LMM) with condition as a fixed effect and biological replicate as a random effect, implemented in R (lmerTest package). Effect sizes (Cohen's d) and estimated marginal means (EMMs) with 95% confidence intervals (CI) were computed; skewness (γ) was reported per condition.

Colocalization between αS and MAM puncta was quantified using object-based analysis on pre-segmented ROIs generated by the FWHM-based approach. Area-overlap coefficients (M1, M2) and Jaccard index were calculated. Statistical reliability was assessed by Monte Carlo randomization (1000 iterations). Observed values were compared to randomized distributions using Student's t-test. Comparisons between conditions were performed using one-way ANOVA (M1) or Kruskal-Wallis test (M2), and figures were generated in GraphPad Prism (v11.0.0).

Endolysosomal pool. For endolysosomal pool quantifications in fixed cells, total intensities of Lamp1 and Rab5 antibody signal were measured within ROI-masked cell areas, respectively. Mean Lamp1/Rab5 intensity ratio, or mean individual channel intensities were plotted per-image. For LysoSensor intensity data, individual endolysosomal compartment ROIs were manually generated in SymphoTime. For αS-treated conditions, endolysosomal puncta were separated into αS-associated (spatially overlapping with αS signal) or αS-distal (remaining compartments). In untreated control cells, all endolysosomal puncta were kept pooled. Mean fluorescence intensity per ROI was extracted in Fiji, providing a size-independent measure of LysoSensor signal per organelle.

Mitochondrial morphology analysis. Mitochondrial morphology and network connectivity was quantified from single-plane using a pipeline combining manual segmentation in Cellpose with automated morphometric analysis in Fiji. Images from SH-SY5Y, αS-SNAP cell lines, and DNeurons were processed with cell-type-specific parameters, held constant across all conditions and experiments of a given cell line. **MitochondriaAnalyzer.** Images were background subtracted, cell-soma and mitochondrial masks were generated as stated above. Mitochondrial ROIs were refined by clearing pixel intensities outside the ROI boundaries in Fiji. These were processed with the Mitochondria Analyzer plugin for Fiji[83] (v2.3.0) using the 2D Threshold and 2D Analysis modules in batch mode via an in-house Fiji macro. From MitochondriaAnalyzer, two metrics were used for downstream analysis: (i) the mean mitochondrial branch length per image, (ii) the mean aspect ratio (AR) per image. **Analyze Particles.** To quantify mitochondria vesicle density per cell area or total mitochondria (vesicles per 1000 µm²), a complementary particle-based analysis was performed on binary mitochondrial masks using a custom Fiji-macro. Particle analysis was performed using Fiji's Analyze Particles function restricted to the per-image combined cell-soma ROI, with a circularity range of 0.50–1.00 and a size range of typically 0.3–∞ µm² (reference: smallest to largest vesicle in control sample, varied between data sets). Mitochondria vesicle density and mean branch length data were min–max normalized across all conditions within each biological replicate prior to pooling. Aspect ratio remained unnormalized. Metrics were computed on per-image basis, with one image representing one data point. Timelapses were generated using the concatenate function in Fiji.

Mitochondrial transfer assay. For each channel, per-image total fluorescence intensity was assessed in Fiji, restricted to cell soma marked regions. Channels analysed: MitoTracker Green for astrocytic uptake of neuronal mitochondria, MitoTracker Red CMXRos for neuronal uptake of astrocytic mitochondria, or PicoGreen for astrocytic uptake of neuronal. Data was normalized to the total nuclei count per image. Per biological replicate, values were normalized to the mean of the H_2O_2-treated control.

Statistical analysis

Outlier detection was performed per condition × replicate in python, combining standard Tukey IQR fences and a modified z-score based on the median absolute deviation (MAD). Data points flagged by both methods were excluded.

Graphs were generated in GraphPad Prism 11 (11.0.0). Data was normalized across all conditions within each biological replicate prior to pooling, either by min.-max. normalization or by transformation to mean of controls. Statistical analysis was performed with GraphPad Prism or in R. Applied statistical tests were determined by normality and lognormality test results. For comparison of two groups two-tailed Student's t test was performed, for comparison of multiple groups by ordinary one-way ANOVA with post hoc Dunnett's or Tukey' HSD comparison, or Kruskal-Wallis test with post hoc Dunn's comparison. Individual punctum-level measurements of endolysosomal LysoSensor intensity and per-organelle MAM size were subjected to linear mixed models (LMM) analysis with the formula: Value ~ Condition + (1|Replicate/Image), fitted by restricted maximum likelihood using the lmerTest package (v3.2.0) in R (v4.5.2). Satterthwaite's method was used for denominator degrees of freedom and Kenward-Roger correction for estimated marginal means (emmeans package, v2.0.1) and post-hoc comparisons were assessed with Tukey HSD correction. For both datasets, individual images were nested within biological replicates as a random effect. Due to the present number of biological replicates (n = 2–4 replicates per condition due to unbalanced factorial design), effect sizes (Cohen's d) and estimated marginal means (EMMs) with 95% confidence intervals are reported rather than p-values alone. Distribution skewness (γ) was computed per condition and per replicate as a descriptive measure of subpopulation effects. The number of experimental replicates and the p-values can be found in the figure legends for each experiment.

Data availability

The proteomic raw datasets generated for this study are available.

Code availability

Custom Fiji macros (RS-FISH batch detection, FWHM-based ROI expansion), Python scripts (stacked line profiles, IQR and size-range-based outlier removal, chromatic aberration correction, colocalization analysis), and R scripts (LMM statistics) are available upon request.

References

1. Jucker, M. & Walker, L. C. Self-propagation of pathogenic protein aggregates in neurodegenerative diseases. *Nature* **501**, 45–51 (2013).
2. Wilson, D. M. *et al.* Hallmarks of neurodegenerative diseases. *Cell* **186**, 693–714 (2023).
3. Braak, H. *et al.* Staging of brain pathology related to sporadic Parkinson's disease. *Neurobiol. Aging* **24**, 197–211 (2003).
4. Luk, K. C. *et al.* Pathological α-Synuclein Transmission Initiates Parkinson-like Neurodegeneration in Non-transgenic Mice. *Science* **338**, 949–953 (2012).

5. Henderson, M. X. *et al.* α-Synuclein pathology spread through the brain connectome is modulated by selective vulnerability and predicted by network analysis. *Nat. Neurosci.* **22**, 1248–1257 (2019).
6. Lee, H.-J., Patel, S. & Lee, S.-J. Intravesicular Localization and Exocytosis of α-Synuclein and its Aggregates. *J. Neurosci.* **25**, 6016–6024 (2005).
7. Desplats, P. *et al.* Inclusion formation and neuronal cell death through neuron-to-neuron transmission of α-synuclein. *Proc. Natl. Acad. Sci. U. S. A.* **106**, 13010–13015 (2009).
8. Abounit, S. *et al.* Tunneling nanotubes spread fibrillar α-synuclein by intercellular trafficking of lysosomes. *EMBO J.* **35**, 2120–2138 (2016).
9. Emmanouilidou, E. *et al.* Cell-Produced α-Synuclein Is Secreted in a Calcium-Dependent Manner by Exosomes and Impacts Neuronal Survival. *J. Neurosci.* **30**, 6838–6851 (2010).
10. Mao, X. *et al.* Pathological α-synuclein transmission initiated by binding lymphocyte-activation gene 3. *Science* **353**, aah3374 (2016).
11. Birol, M., Wojcik, S. P., Miranker, A. D. & Rhoades, E. Identification of N-linked glycans as specific mediators of neuronal uptake of acetylated α-Synuclein. *PLOS Biol.* **17**, e3000318 (2019).
12. Lee, H.-J. *et al.* Direct Transfer of α-Synuclein from Neuron to Astroglia Causes Inflammatory Responses in Synucleinopathies. *J. Biol. Chem.* **285**, 9262–9272 (2010).
13. Borghi, R. *et al.* Full length α-synuclein is present in cerebrospinal fluid from Parkinson's disease and normal subjects. *Neurosci. Lett.* **287**, 65–67 (2000).
14. Mollenhauer, B. *et al.* Direct quantification of CSF α-synuclein by ELISA and first cross-sectional study in patients with neurodegeneration. *Exp. Neurol.* **213**, 315–325 (2008).
15. Mollenhauer, B. *et al.* α-Synuclein and tau concentrations in cerebrospinal fluid of patients presenting with parkinsonism: a cohort study. *Lancet Neurol.* **10**, 230–240 (2011).
16. Eusebi, P. *et al.* Diagnostic utility of cerebrospinal fluid α-synuclein in Parkinson's disease: A systematic review and meta-analysis. *Mov. Disord.* **32**, 1389–1400 (2017).
17. Tanik, S. A., Schultheiss, C. E., Volpicelli-Daley, L. A., Brunden, K. R. & Lee, V. M. Y. Lewy Body-like α-Synuclein Aggregates Resist Degradation and Impair Macroautophagy♦. *J. Biol. Chem.* **288**, 15194–15210 (2013).
18. Karim, Md. R. *et al.* Internalized SNCA/α-synuclein fibrils become truncated and resist degradation in neurons while glial cells rapidly degrade SNCA fibrils. *Autophagy* **22**, 102–120.
19. Yun, S. P. *et al.* Block of A1 astrocyte conversion by microglia is neuroprotective in models of Parkinson's disease. *Nat. Med.* **24**, 931–938 (2018).
20. Lee, H.-J. *et al.* Direct Transfer of α-Synuclein from Neuron to Astroglia Causes Inflammatory Responses in Synucleinopathies. *J. Biol. Chem.* **285**, 9262–9272 (2010).
21. Kim, C. *et al.* Neuron-released oligomeric α-synuclein is an endogenous agonist of TLR2 for paracrine activation of microglia. *Nat. Commun.* **4**, 1562 (2013).
22. Flønes, I. H. *et al.* Mitochondrial complex I deficiency stratifies idiopathic Parkinson's disease. *Nat. Commun.* **15**, 3631 (2024).
23. Toomey, C. E. *et al.* Mitochondrial dysfunction is a key pathological driver of early stage Parkinson's. *Acta Neuropathol. Commun.* **10**, 134 (2022).
24. Herrera-Vaquero, M. *et al.* Signs of early cellular dysfunction in multiple system atrophy. *Neuropathol. Appl. Neurobiol.* **47**, 268–282 (2021).
25. Hatton, C. *et al.* Complex I reductions in the nucleus basalis of Meynert in Lewy body dementia: the role of Lewy bodies. *Acta Neuropathol. Commun.* **8**, 103 (2020).
26. Geibl, F. F. *et al.* α-Synuclein pathology disrupts mitochondrial function in dopaminergic and cholinergic neurons at-risk in Parkinson's disease. *Mol. Neurodegener.* **19**, 69 (2024).

27. Shahmoradian, S. H. *et al.* Lewy pathology in Parkinson's disease consists of crowded organelles and lipid membranes. *Nat. Neurosci.* **22**, 1099–1109 (2019).
28. Nakamura, K. *et al.* Direct Membrane Association Drives Mitochondrial Fission by the Parkinson Disease-associated Protein α-Synuclein *♦. *J. Biol. Chem.* **286**, 20710–20726 (2011).
29. Chen, H., McCaffery, J. M. & Chan, D. C. Mitochondrial Fusion Protects against Neurodegeneration in the Cerebellum. *Cell* **130**, 548–562 (2007).
30. Exner, N. *et al.* Loss-of-Function of Human PINK1 Results in Mitochondrial Pathology and Can Be Rescued by Parkin. *J. Neurosci.* **27**, 12413–12418 (2007).
31. Szabadkai, G. *et al.* Chaperone-mediated coupling of endoplasmic reticulum and mitochondrial Ca2+ channels. *J. Cell Biol.* **175**, 901–911 (2006).
32. Friedman, J. R. *et al.* ER Tubules Mark Sites of Mitochondrial Division. *Science* **334**, 358–362 (2011).
33. Modi, S. *et al.* Miro clusters regulate ER-mitochondria contact sites and link cristae organization to the mitochondrial transport machinery. *Nat. Commun.* **10**, 4399 (2019).
34. Wong, Y. C., Ysselstein, D. & Krainc, D. Mitochondria–lysosome contacts regulate mitochondrial fission via RAB7 GTP hydrolysis. *Nature* **554**, 382–386 (2018).
35. Peng, W., Wong, Y. C. & Krainc, D. Mitochondria-lysosome contacts regulate mitochondrial Ca2+ dynamics via lysosomal TRPML1. *Proc. Natl. Acad. Sci.* **117**, 19266–19275 (2020).
36. Hamasaki, M. *et al.* Autophagosomes form at ER–mitochondria contact sites. *Nature* **495**, 389–393 (2013).
37. Gelmetti, V. *et al.* PINK1 and BECN1 relocalize at mitochondria-associated membranes during mitophagy and promote ER-mitochondria tethering and autophagosome formation. *Autophagy* **13**, 654–669 (2017).
38. Bui, V., Santerre, M., Shcherbik, N. & Sawaya, B. E. Mitochondria-associated membranes (MAMs): molecular organization, cellular functions, and their role in health and disease. *FEBS Open Bio* **16**, 11–24 (2026).
39. Davis, C. O. *et al.* Transcellular degradation of axonal mitochondria. *Proc. Natl. Acad. Sci.* **111**, 9633–9638 (2014).
40. Nicolás-Ávila, J. A. *et al.* A Network of Macrophages Supports Mitochondrial Homeostasis in the Heart. *Cell* **183**, 94-109.e23 (2020).
41. Hayakawa, K. *et al.* Transfer of mitochondria from astrocytes to neurons after stroke. *Nature* **535**, 551–555 (2016).
42. Calì, T., Ottolini, D., Negro, A. & Brini, M. α-Synuclein Controls Mitochondrial Calcium Homeostasis by Enhancing Endoplasmic Reticulum-Mitochondria Interactions*. *J. Biol. Chem.* **287**, 17914–17929 (2012).
43. Guardia-Laguarta, C. *et al.* α-Synuclein Is Localized to Mitochondria-Associated ER Membranes. *J. Neurosci.* **34**, 249–259 (2014).
44. Paillusson, S. *et al.* α-Synuclein binds to the ER–mitochondria tethering protein VAPB to disrupt Ca2+ homeostasis and mitochondrial ATP production. *Acta Neuropathol. (Berl.)* **134**, 129–149 (2017).
45. Barbuti, P. A. *et al.* The role of alpha-synuclein in synucleinopathy: Impact on lipid regulation at mitochondria–ER membranes. *Npj Park. Dis.* **11**, 103 (2025).
46. Narendra, D., Tanaka, A., Suen, D.-F. & Youle, R. J. Parkin is recruited selectively to impaired mitochondria and promotes their autophagy. *J. Cell Biol.* **183**, 795–803 (2008).

47. Brooker, S. M., Naylor, G. E. & Krainc, D. Cell biology of Parkinson's disease: Mechanisms of synaptic, lysosomal, and mitochondrial dysfunction. *Curr. Opin. Neurobiol.* **85**, 102841 (2024).
48. Rustom, A., Saffrich, R., Markovic, I., Walther, P. & Gerdes, H.-H. Nanotubular Highways for Intercellular Organelle Transport. *Science* **303**, 1007–1010 (2004).
49. Spees, J. L., Olson, S. D., Whitney, M. J. & Prockop, D. J. Mitochondrial transfer between cells can rescue aerobic respiration. *Proc. Natl. Acad. Sci.* **103**, 1283–1288 (2006).
50. Islam, M. N. *et al.* Mitochondrial transfer from bone-marrow–derived stromal cells to pulmonary alveoli protects against acute lung injury. *Nat. Med.* **18**, 759–765 (2012).
51. Court, A. C. *et al.* Mitochondrial transfer from MSCs to T cells induces Treg differentiation and restricts inflammatory response. *EMBO Rep.* **21**, EMBR201948052 (2020).
52. Tan, A. S. *et al.* Mitochondrial Genome Acquisition Restores Respiratory Function and Tumorigenic Potential of Cancer Cells without Mitochondrial DNA. *Cell Metab.* **21**, 81–94 (2015).
53. Ikeda, H. *et al.* Immune evasion through mitochondrial transfer in the tumour microenvironment. *Nature* **638**, 225–236 (2025).
54. Cai, J. *et al.* Aerobic exercise improves astrocyte mitochondrial quality and transfer to neurons in a mouse model of Alzheimer's disease. *Brain Pathol.* **35**, e13316 (2025).
55. Cheng, X.-Y. *et al.* Human iPSCs derived astrocytes rescue rotenone-induced mitochondrial dysfunction and dopaminergic neurodegeneration in vitro by donating functional mitochondria. *Transl. Neurodegener.* **9**, 13 (2020).
56. Physiology of Astroglia | Physiological Reviews | American Physiological Society. *Physiol. Rev.* https://journals.physiology.org/doi/10.1152/physrev.00042.2016.
57. Boutry, M. & Kim, P. K. ORP1L mediated PI(4)P signaling at ER-lysosome-mitochondrion three-way contact contributes to mitochondrial division. *Nat. Commun.* **12**, 5354 (2021).
58. Elbaz-Alon, Y. *et al.* PDZD8 interacts with Protrudin and Rab7 at ER-late endosome membrane contact sites associated with mitochondria. *Nat. Commun.* **11**, 3645 (2020).
59. Vallese, F. *et al.* An expanded palette of improved SPLICS reporters detects multiple organelle contacts in vitro and in vivo. *Nat. Commun.* **11**, 6069 (2020).
60. Phillips, M. J. & Voeltz, G. K. Structure and function of ER membrane contact sites with other organelles. *Nat. Rev. Mol. Cell Biol.* **17**, 69–82 (2016).
61. King, C., Sengupta, P., Seo, A. Y. & Lippincott-Schwartz, J. ER membranes exhibit phase behavior at sites of organelle contact. *Proc. Natl. Acad. Sci.* **117**, 7225–7235 (2020).
62. Schöller, E. *et al.* Balancing of mitochondrial translation through METTL8-mediated m3C modification of mitochondrial tRNAs. *Mol. Cell* **81**, 4810-4825.e12 (2021).
63. Hallacli, E. *et al.* The Parkinson's disease protein alpha-synuclein is a modulator of processing bodies and mRNA stability. *Cell* **185**, 2035-2056.e33 (2022).
64. Gäbelein, C. G. *et al.* Mitochondria transplantation between living cells. *PLOS Biol.* **20**, e3001576 (2022).
65. Lautenschläger, J. *et al.* C-terminal calcium binding of α-synuclein modulates synaptic vesicle interaction. *Nat. Commun.* **9**, 712 (2018).
66. Raiborg, C. *et al.* Repeated ER–endosome contacts promote endosome translocation and neurite outgrowth. *Nature* **520**, 234–238 (2015).
67. Chu, Q. *et al.* Regulation of the ER stress response by a mitochondrial microprotein. *Nat. Commun.* **10**, 4883 (2019).
68. Afitska, K., Fucikova, A., Shvadchak, V. V. & Yushchenko, D. A. α-Synuclein aggregation at low concentrations. *Biochim. Biophys. Acta BBA - Proteins Proteomics* **1867**, 701–709 (2019).

69. Hartfield, E. M. *et al.* Physiological Characterisation of Human iPS-Derived Dopaminergic Neurons. *PLOS ONE* **9**, e87388 (2014).
70. Alisch, M. *et al.* Identification of the gliogenic state of human neural stem cells to optimize in vitro astrocyte differentiation. *J. Neurosci. Methods* **361**, 109284 (2021).
71. Kerkering, J. *et al.* iPSC-derived reactive astrocytes from patients with multiple sclerosis protect cocultured neurons in inflammatory conditions. *J. Clin. Invest.* **133**, (2023).
72. Trexler, A. J. & Rhoades, E. N-terminal acetylation is critical for forming α-helical oligomer of α-synuclein. *Protein Sci.* **21**, 601–605 (2012).
73. Birol, M., Mu, ñoz I. I. D., Rhoades, E. & Lippincott, -Schwartz Jennifer. The C-terminus of α-Synuclein Regulates its Dynamic Cellular Internalization by Neurexin 1β. *Mol. Biol. Cell* **34**, br21 (2023).
74. Bruderer, R. *et al.* Extending the Limits of Quantitative Proteome Profiling with Data-Independent Acquisition and Application to Acetaminophen-Treated Three-Dimensional Liver Microtissues *[S]. *Mol. Cell. Proteomics* **14**, 1400–1410 (2015).
75. Ritchie, M. E. *et al.* limma powers differential expression analyses for RNA-sequencing and microarray studies. *Nucleic Acids Res.* **43**, e47 (2015).
76. Durinck, S. *et al.* BioMart and Bioconductor: a powerful link between biological databases and microarray data analysis. *Bioinformatics* **21**, 3439–3440 (2005).
77. Wu, T. *et al.* clusterProfiler 4.0: A universal enrichment tool for interpreting omics data. *The Innovation* **2**, 100141 (2021).
78. Rath, S. *et al.* MitoCarta3.0: an updated mitochondrial proteome now with sub-organelle localization and pathway annotations. *Nucleic Acids Res.* **49**, D1541–D1547 (2021).
79. Lowekamp, B. C., Chen, D. T., Ibanez, L. & Blezek, D. The Design of SimpleITK. *Front. Neuroinformatics* **7**, (2013).
80. Stringer, C., Wang, T., Michaelos, M. & Pachitariu, M. Cellpose: a generalist algorithm for cellular segmentation. *Nat. Methods* **18**, 100–106 (2021).
81. Stringer, C. & Pachitariu, M. Cellpose3: one-click image restoration for improved cellular segmentation. *Nat. Methods* **22**, 592–599 (2025).
82. Bahry, E. *et al.* RS-FISH: precise, interactive, fast, and scalable FISH spot detection. *Nat. Methods* **19**, 1563–1567 (2022).
83. Chaudhry, A., Shi, R. & Luciani, D. S. A pipeline for multidimensional confocal analysis of mitochondrial morphology, function, and dynamics in pancreatic β-cells. *Am. J. Physiol. Endocrinol. Metab.* **318**, E87–E101 (2020).

Author contribution

M.B and E.F conceptualized the study and designed the experiments, E.F performed, analyzed and curated the data for most the experiments of the study, supervised by M.B and with contributions from: K.H analyzed and curated proteomic data, P.S.O performed the western blots, helped with stainings and supported neuronal differentiations, T.K prepared samples and performed mass spectrometry, and ran limma analyses, supervised by I.P, C.B supervised the FAOS, J. R performed imaging for stainings and FAOS preparation and differentiation of human astrocytes, L.B set up the pipeline for chromatic shift correction and RS-FISH spot-detection. M.B provided funding acquisition. E.F and M.B wrote the original draft and all authors participated in the review process.

Acknowledgements

We thank all members of the Birol laboratory for their support, insightful discussions, feedback, and continuous encouragement throughout this project. We thank Erich Wanker, Oliver Daumke, Johannes Broichhagen for valuable feedback, discussions, and advice during the development of this work. We also thank Johannes Broichhagen and Katja Simon for advice on the manuscript. We also thank the Siffrin laboratory for sharing astrocyte differentiation protocols. We acknowledge the support of the Systems Biology imaging platform at MDC, for microscopy assistance and technical expertise.

Figure 1

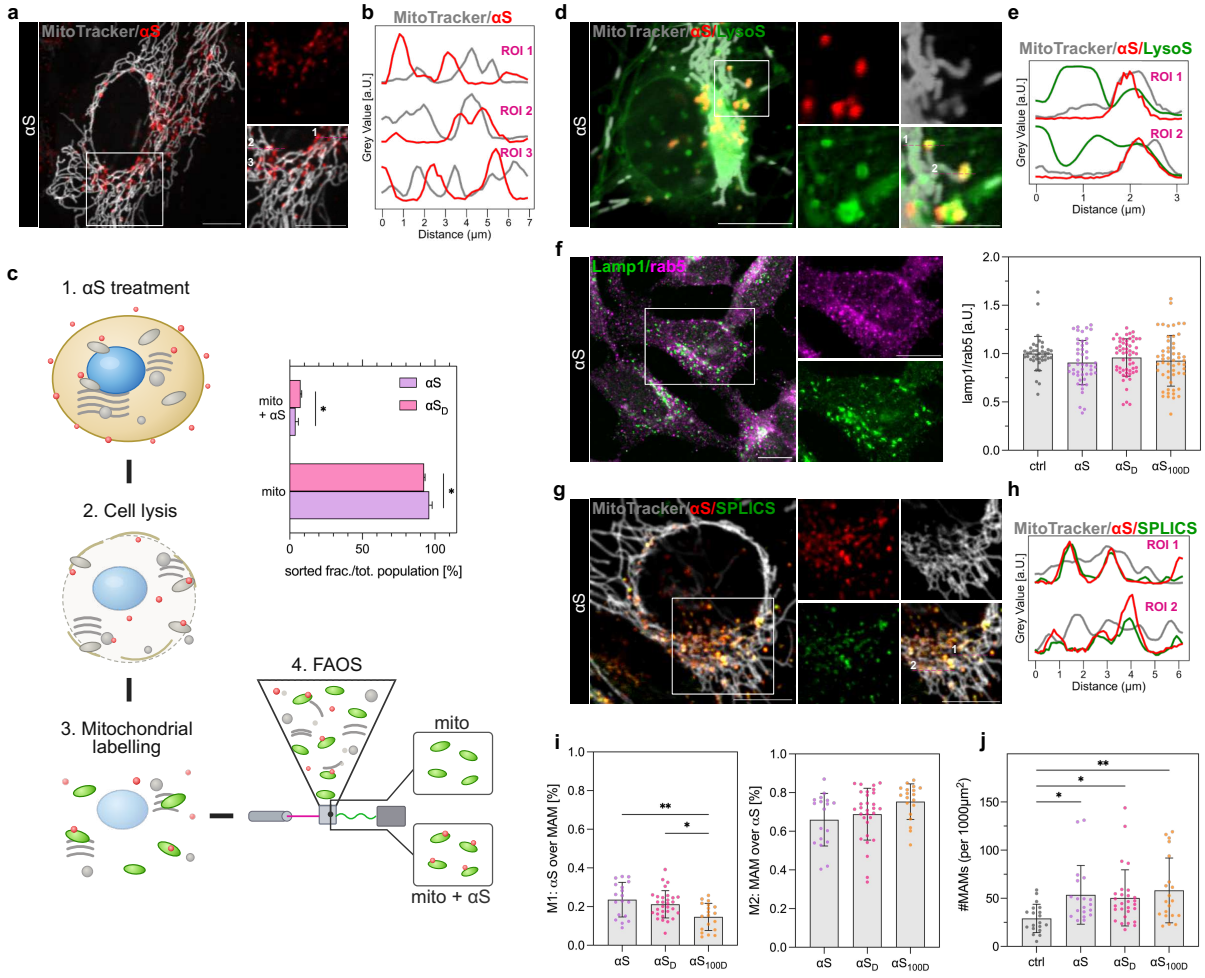

Figure 1. Internalized monomeric αS localizes to mitochondria and tri-organelle contact sites.

a, Representative confocal images of SH-SY5Y cells labeled with MitoTracker (grey) following treatment with αS (red). Insets highlight regions of mitochondria-associated αS puncta.

b, Fluorescence intensity line profiles across selected regions of interest (ROIs) from (a) showing αS puncta in close apposition to, but only partial overlap with mitochondria.

c, Schematic of FAOS workflow for isolation of mitochondria. SH-SY5Y were treated with αS, lysed, and MitoTracker-labeled mitochondria were sorted from whole cell-lysates into αS-positive ($αS^+$) and αS-negative ($αS^-$) sub-populations for downstream analysis. Fractions of $αS^+$ and $αS^-$ mitochondria of total sorted population shown in quantification. Unpaired two-tailed t-test with Welch's correction. *N=2-4* biological replicates; total sorted single events ranged from ~36000 to 290000.

d, Confocal images of DNeurons labeled with MitoTracker, αS, and LysoSensor (green), revealing frequent localization of mitochondria-associated αS puncta with endolysosomal compartments. Insets highlight regions containing mitochondria, αS and endolysosomes.

e, Intensity line profiles of ROIs from (d) demonstrating overlap between αS and LysoSensor-positive compartments adjacent to mitochondria.

f, Immunofluorescence images of SH-SY5Y co-stained for late endosomal-lysosomal (Lamp1) and early endosomal (Rab5) markers. Lamp1/Rab5 fluorescence intensity ratio is unchanged across all conditions

indicating that αS treatment does not affect endolysosomal pool composition. Kruskal-Wallis with Dunn's post-hoc. *N*=5-7 replicates.

g, Representative images of SH-SY5Y expressing MAM-marker SPLICS (green), together with MitoTracker and αS. Insets highlight αS-MAM localization.

h, Intensity line profiles of ROIs from (g) demonstrating colocalization of αS with SPLICS-positive contact sites.

i, Object-based colocalization analysis of αS with SPLICS. M1 (fraction: αS overlapping MAM) was significantly reduced for αS_{100D}. M2 (fraction: MAM overlapping αS) showed no significant difference across αS variants. Ordinary one-way-Anova with post hoc Tukey's. *N*=2-3 biological replicates.

j, Density of SPLICS-positive MAM contact sites per 1000 μm² cell area. αS treatment increased MAM density compared to untreated control, with no significant differences detected between αS variants. Kruskal-Wallis with Dunn's post-hoc. *N=2-3* biological replicates.

Data are presented as mean ± s.e.m: each point represents a single FOV. * $p < 0.05$, ** $p < 0.01$). Scale bars: a, d, f, g, 10 μm; d inset, 5 μm.

Figure S1

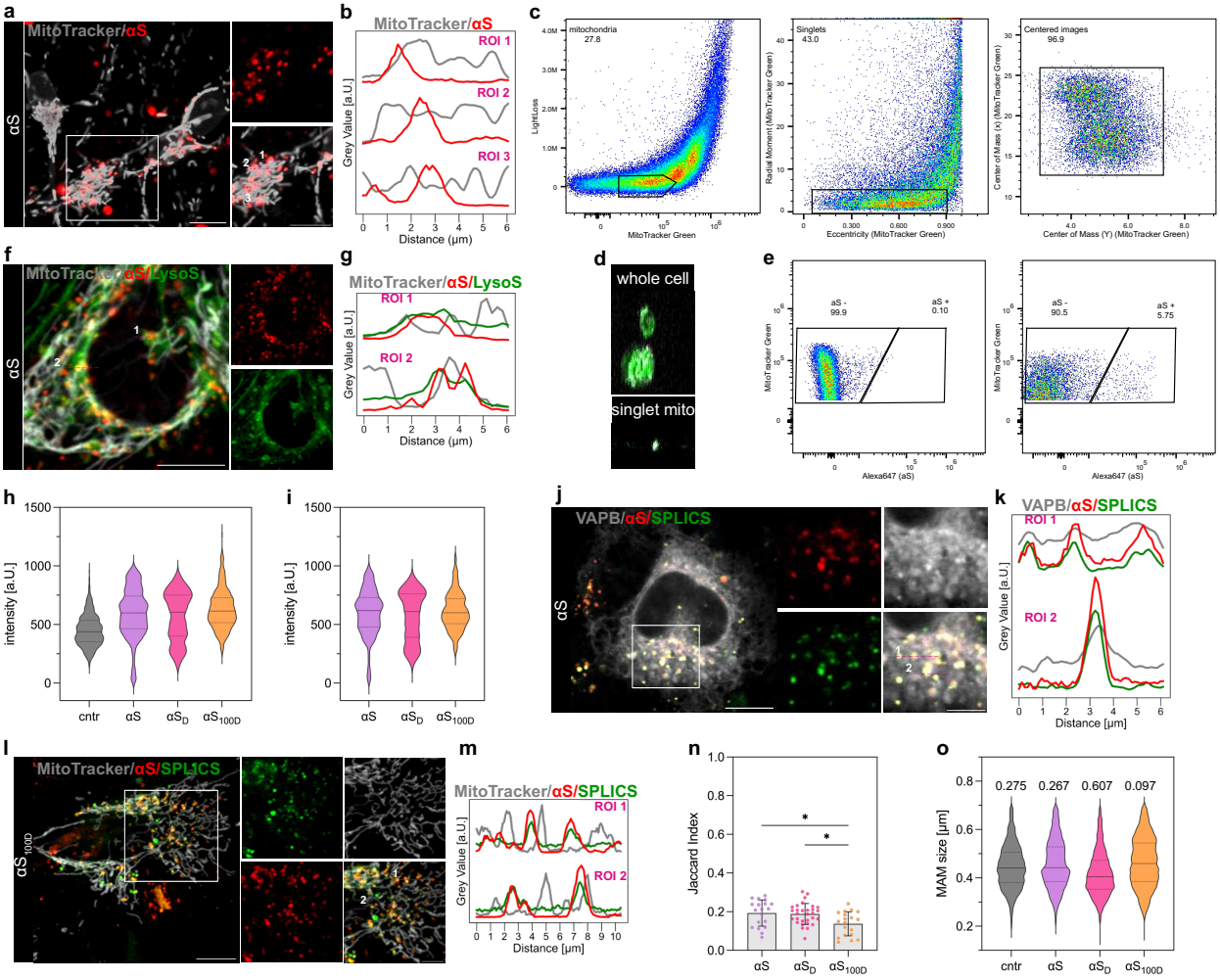

Figure S1. Subcellular distribution and compartmental characterization of internalized αS.

a, Representative images of DNeurons labeled with MitoTracker (grey) following αS (red) treatment. Insets highlight regions of close spatial association.

b, Intensity line profiles across selected ROIs from (a).

c, Representative density plots show sequential gating of mitochondrial events based on MitoTracker Green versus axial light loss (P1), eccentricity versus radial moment (P2), and centre-of-mass position (P3). Percentages indicate the fraction of events retained at each gate.

d, Representative BD CellView images confirming selection of individual mitochondria. Top: intact cells in lysate before gating. Bottom: a morphologically defined mitochondrial singlet retained after the P1–P3 gating strategy.

e, Representative FAOS density plots showing gating of αS^-/MitoTracker$^+$ and αS^+/MitoTracker$^+$ mitochondrial fractions based on MitoTracker Green and Alexa647 fluorescence. Percentages indicate gated events.

f, Confocal images of SH-SY5Y cells with MitoTracker, αS, and LysoSensor (green). Insets highlight αS and endolysosomes.

g, Intensity line profiles from ROIs in (f).

h, i, Quantification of LysoSensor fluorescence intensity in DNeuron endolysosomes. h, Total endolysosomal pool. i, αS-associated endolysosomes. LMM with nested random effects

(1|Replicate/Image), Tukey HSD post-hoc, lmerTest. *N*=2-3 biological replicates; 6-9 FOV and 95-530 puncta per condition, per ROI.
j, Confocal images of SH-SY5Y expressing SPLICS (green) and VAPB (grey) and conditioned with αS (red). Insets highlight regions of colocalization.
k, Intensity line profiles from ROIs in (j).
l, Representative confocal images of SH-SY5Y with MitoTracker, αS_{100D}, and expressing SPLICS (green). Insets show contact regions.
m, Intensity line profiles from ROIs in (l).
n, Jaccard index of object-based colocalization between αS and SPLICS. Ordinary one-way-Anova with post hoc Tukey's. *N*=2-3 biological replicates.
o, MAM contact site radius (µm). αS_D increased distribution skewness (αS_D $\gamma = 0.603$ vs ctrl $\gamma = 0.275$), whereas αS_{100D} showed the lowest skewness ($\gamma = 0.096$). LMM with nested random effects (1|Replicate/Image), lmerTest; *N*=2 biological replicates. Skewness was calculated on image-mean-residualized values.
Bar plots show mean ± s.e.m.; each point represents one FOV. *P < 0.05. Scale bars: a, f, j, l, 10 µm; insets j, l, 5 µm. Violin plots show individual data distributions with median and interquartile range.

Figure 2

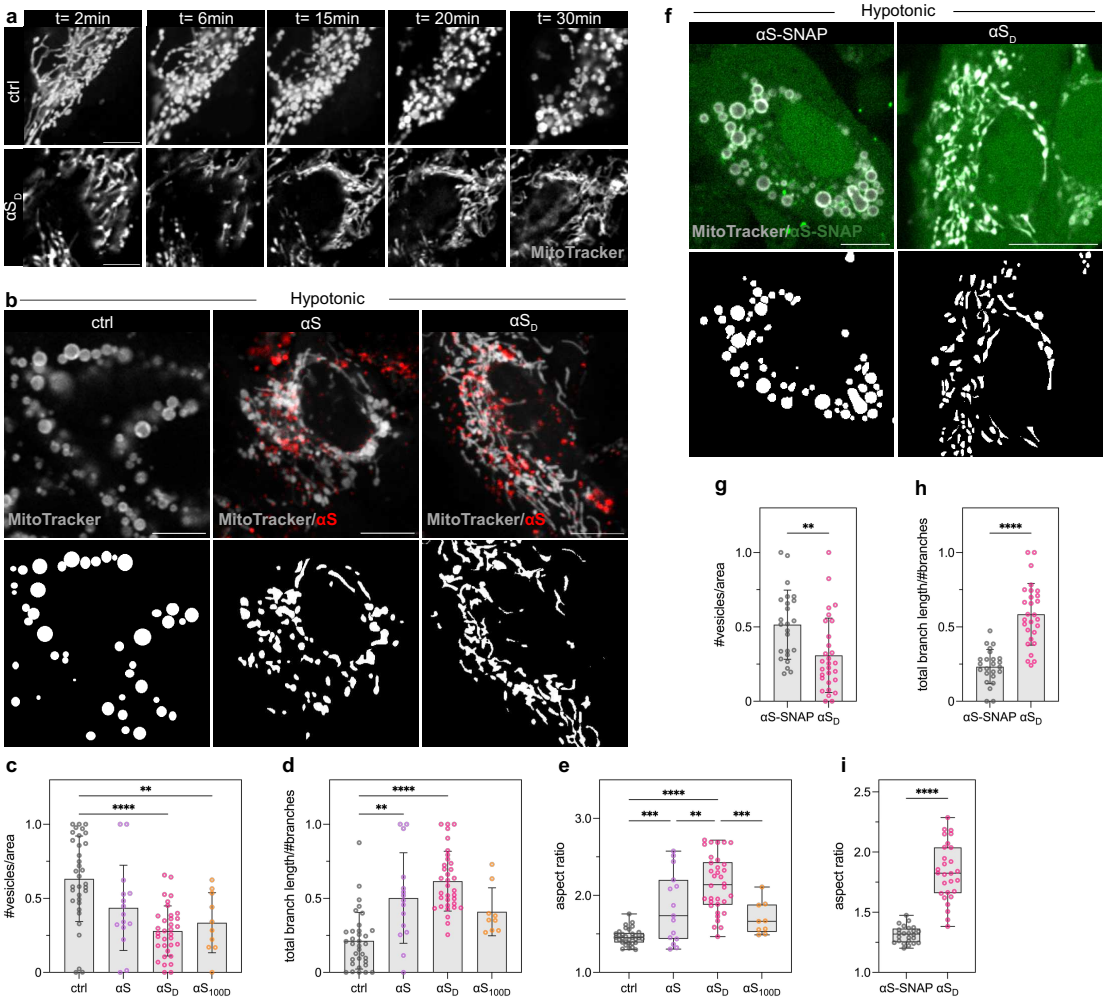

Figure 2. Spreading αS constrains mitochondrial remodeling and organelle plasticity.

a, Time-lapse confocal imaging of mitochondria after hypotonic treatment in ctrl and αS_D-treated SH-SY5Y cells. Representative frames show mitochondrial network dynamics over time (2–30 min post-hypotonic treatment), revealing reduced mitochondrial remodeling and motility in αS_D.

b, Representative images of mitochondria ~30 min post-hypotonic swelling, visualized by MitoTracker in ctrl and αS_D cells. Bottom panels show corresponding segmentation of mitochondria.

c-e, Quantifications of mitochondria morphology after hypotonic swelling, comparing the number of LICVs per cell area (c), mean branch length (d), and mitochondria tubule elongation (aspect ratio, e), between ctrl and αS conditions. αS exposure impairs mitochondrial vesiculation, in a concentration- and C-terminal-dependent manner. Ordinary one-way-Anova with Tukey's post-hoc. *N*=2-5 biological replicates.

f, Representative images of LICVs in αS-SNAP overexpressing SH-SY5Y cells under hypotonic conditions. Conditioning with αS_D shows impaired mitochondrial vesiculation.

g-i, Quantification of mitochondria morphology post-hypotonic treatment of αS-SNAP overexpressing SH-SY5Y cells, conditioned with- (denoted αS_D) and without-(denoted αS-SNAP) αS_D. Unpaired two-tailed Student's t-test or Mann-Whitney. *N*=2 biological replicates.

Data are mean ± s.e.m.; each point represents one cell or FOV. * $p < 0.05$, ** $p < 0.01$, *** $p < 0.001$, **** $p < 0.0001$. Scale bars: 10 µm.

Figure S2

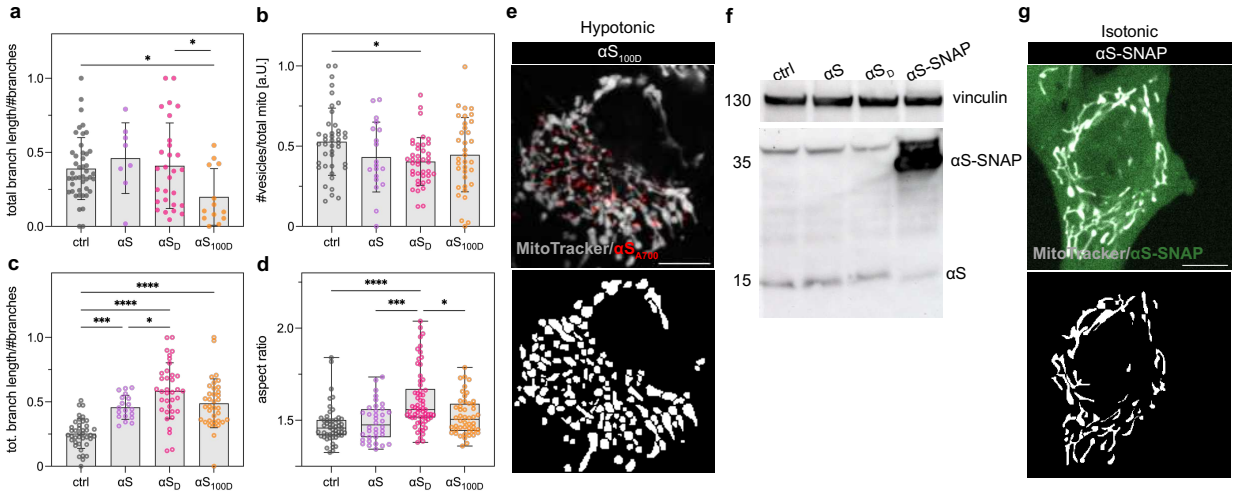

Figure S2. Spreading αS constrains mitochondrial remodeling in a C-terminal-dependent manner and independently of intracellular αS expression.

a, Quantification of mitochondrial mean branch length under homeostatic (isotonic) conditions across conditions. αS does not show significant alterations, while αS_{100D} shows reduced branch length under homeostatic conditions. Ordinary one-way-Anova with Dunnett's post-hoc. *N=2-3* biological replicates.

b-d, Quantification of mitochondria morphology post-hypotonic treatment in control and αS-treated DNeurons. The number of LICVs shows a significant reduction in the αS_D condition (b), while mean branch length (c) and branch elongation (d) are significantly increased in a concentration- and C-terminal-dependent manner. Ordinary one-way-Anova with Tukey's or Kruskal-Wallis with Dunn's post-hoc. *N=2* biological replicates.

e, Representative image and segmentation mask of mitochondria in αS_{100D}-treated SH-SY5Y cells under hypotonic conditions.

f, Western blot of cell lysates from ctrl, αS-treated (αS, αS_D), and αS-SNAP-overexpressing SH-SY5Y cells, probed with anti-αS and anti-SNAP antibodies. Vinculin was used as a loading control.

g, Representative confocal image and binary mask of αS-SNAP expressing SH-SY5Y cells under isotonic conditions.

Data are mean ± s.e.m.; each point represents one cell or FOV. * $p < 0.05$, ** $p < 0.01$, *** $p < 0.001$, **** $p < 0.0001$. Filled markers: isotonic; open markers: hypotonic. Scale bars: 10 µm.

Figure 3

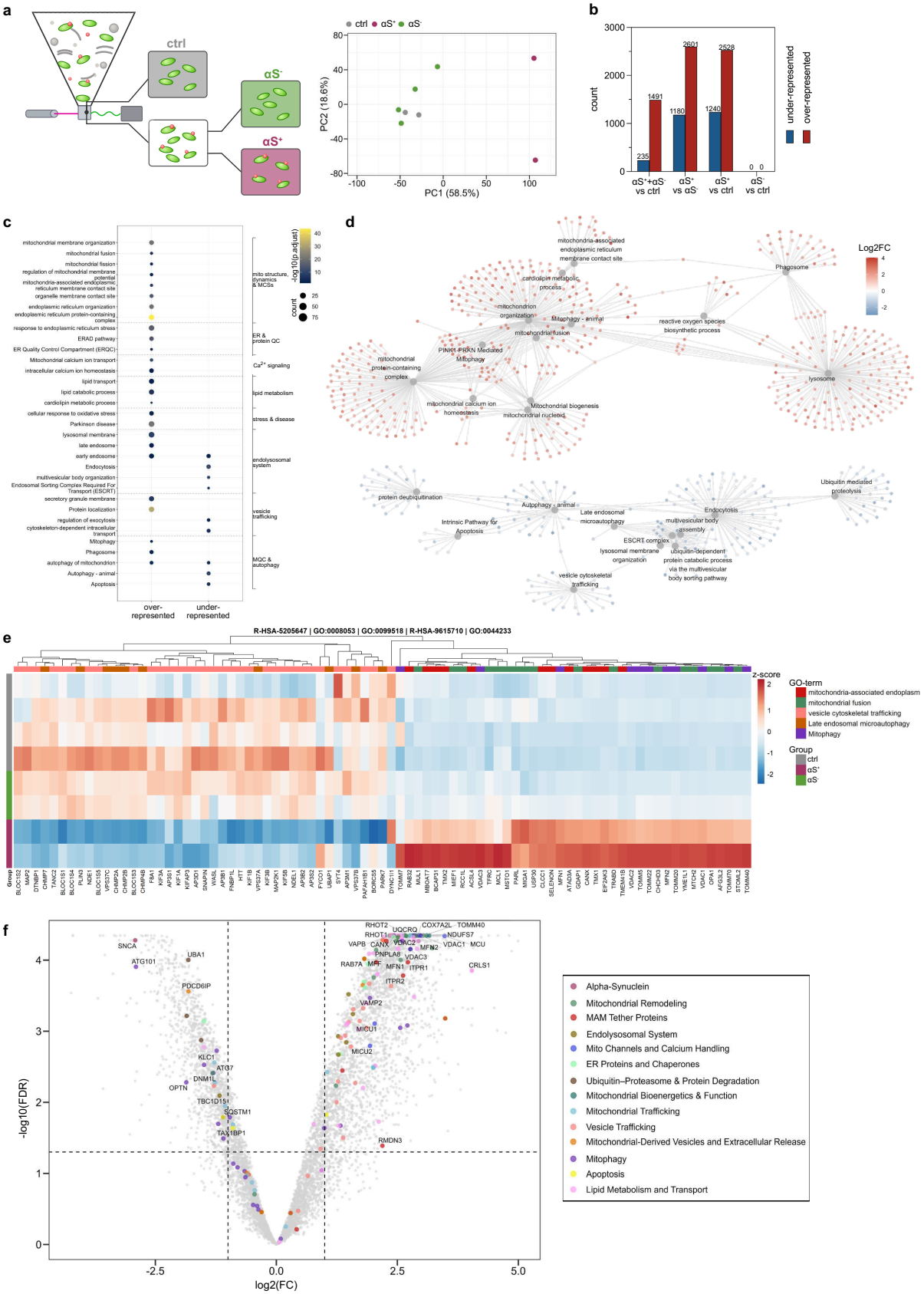
a
ctrl
αS⁻
αS⁺
ctrl αS⁺ αS⁻
PC2 (18.6%)
PC1 (58.5%)
b
count
under-represented
over-represented
1491
2601
1180
1240
2528
235
0 0
αS⁺+αS⁻ vs ctrl
αS⁺ vs αS⁻
αS⁺ vs ctrl
αS⁻ vs ctrl
c
mitochondrial membrane organization
mitochondrial fusion
mitochondrial fission
regulation of mitochondrial membrane potential
mitochondria-associated endoplasmic reticulum membrane contact site
organelle membrane contact site
endoplasmic reticulum organization
endoplasmic reticulum protein-containing complex
response to endoplasmic reticulum stress
ERAD pathway
ER Quality Control Compartment (ERQC)
Mitochondrial calcium ion transport
intracellular calcium ion homeostasis
lipid transport
lipid catabolic process
cardiolipin metabolic process
cellular response to oxidative stress
Parkinson disease
lysosomal membrane
late endosome
early endosome
Endocytosis
multivesicular body organization
Endosomal Sorting Complex Required For Transport (ESCRT)
secretory granule membrane
Protein localization
regulation of exocytosis
cytoskeleton-dependent intracellular transport
Mitophagy
Phagosome
autophagy of mitochondrion
Autophagy - animal
Apoptosis
mito structure, dynamics & MCSs
ER & protein QC
Ca2+ signaling
lipid metabolism
stress & disease
endolysosomal system
vesicle trafficking
MQC & autophagy
-log10(p.adjust)
count
over-represented
under-represented
d
mitochondria-associated endoplasmic reticulum membrane contact site
cardiolipin metabolic process
mitochondrion organization
Mitophagy - animal
mitochondrial fusion
PINK1-PRKN Mediated Mitophagy
mitochondrial protein-containing complex
mitochondrial calcium ion homeostasis
Mitochondrial biogenesis
mitochondrial nucleoid
Phagosome
reactive oxygen species biosynthetic process
lysosome
Log2FC
protein deubiquitination
Autophagy - animal
Intrinsic Pathway for Apoptosis
Late endosomal microautophagy
Endocytosis
multivesicular body assembly
ESCRT complex
lysosomal membrane organization
ubiquitin-dependent protein catabolic process via the multivesicular body sorting pathway
vesicle cytoskeletal trafficking
Ubiquitin mediated proteolysis
e
R-HSA-5205647 | GO:0008053 | GO:0099518 | R-HSA-9615710 | GO:0044233
z-score
GO-term
mitochondria-associated endoplasm
mitochondrial fusion
vesicle cytoskeletal trafficking
Late endosomal microautophagy
Mitophagy
Group
ctrl
αS⁺
αS⁻
f
-log10(FDR)
log2(FC)
SNCA
ATG101
UBA1
PDCD6IP
KLC1
ATG7
DNM1L
OPTN
TBC1D15
SQSTM1
TAX1BP1
RMDN3
RHOT2
UQCRQ
COX7A2L
TOMM40
RHOT1
NDUFS7
VAPB
CANX
VDAC2
MFN2
VDAC1
MCU
PNPLA8
VDAC3
RAB7A
MFF
MFN1
ITPR1
CRLS1
ITPR2
VAMP2
MICU1
MICU2
Alpha-Synuclein
Mitochondrial Remodeling
MAM Tether Proteins
Endolysosomal System
Mito Channels and Calcium Handling
ER Proteins and Chaperones
Ubiquitin–Proteasome & Protein Degradation
Mitochondrial Bioenergetics & Function
Mitochondrial Trafficking
Vesicle Trafficking
Mitochondrial-Derived Vesicles and Extracellular Release
Mitophagy
Apoptosis
Lipid Metabolism and Transport

Figure 3. Spreading αS defines a contact-site–enriched mitochondrial proteome with altered metabolic and quality-control pathways.

a, FAOS workflow for proteomic profiling of mitochondrial subpopulations. Mitochondria were isolated from control cells (ctrl) and αS-treated cells and separated into αS-associated (αS^+) and non-associated (αS^-) fractions. PCA shows a distinct proteomic profile for αS^+ mitochondria compared with ctrl and αS^- fractions.

b, Quantification of differentially abundant proteins across comparisons. Bar plot shows the number of over- and under-represented proteins in $\alpha S^+/\alpha S^-$ vs ctrl, αS^+ vs ctrl, αS^+ vs αS^- and αS^- vs ctrl comparisons. αS^+ mitochondria exhibit extensive proteomic changes relative to ctrl and αS^-, while αS^- vs ctrl shows zero changes.

c, ORA dot plot showing pathway terms concordantly over- and under-represented in αS^+ mitochondria across both αS^+ vs ctrl and αS^+ vs αS^- comparisons. This identified pathways robustly associated with the αS^+ proteomic state, consistent with GSEA (Fig. S3b).

d, Cnet plot of leading-edge proteins from selected GSEA-enriched pathways (αS^+ vs ctrl). Proteins associated with mitochondrial dynamics, morphology, and early MQC processes cluster separately from proteins involved in vesicle trafficking, autophagy, and degradative mitophagy pathways, with no overlap between the two networks.

e, Heatmap of leading-edge proteins from selected pathway terms shown in the cnet analysis (d) across all conditions (ctrl, αS^-, αS^+; rows represent biological replicates). Columns represent individual proteins grouped and color-coded by pathway. Hierarchical clustering confirms the separation of positively and negatively enriched pathways.

f, f, Volcano plot of the αS^+ versus ctrl proteome. Significantly altered proteins are shown in grey, while selected proteins of interest are highlighted and grouped into curated functional categories. Annotated proteins are referenced in the Results section. Dashed lines indicate significance thresholds (adjusted $p < 0.05$; $|\log_2 FC| > 1$). Biological replicates, ctrl, αS, $N=4$; αS_D, $N=2$.

Figure S3

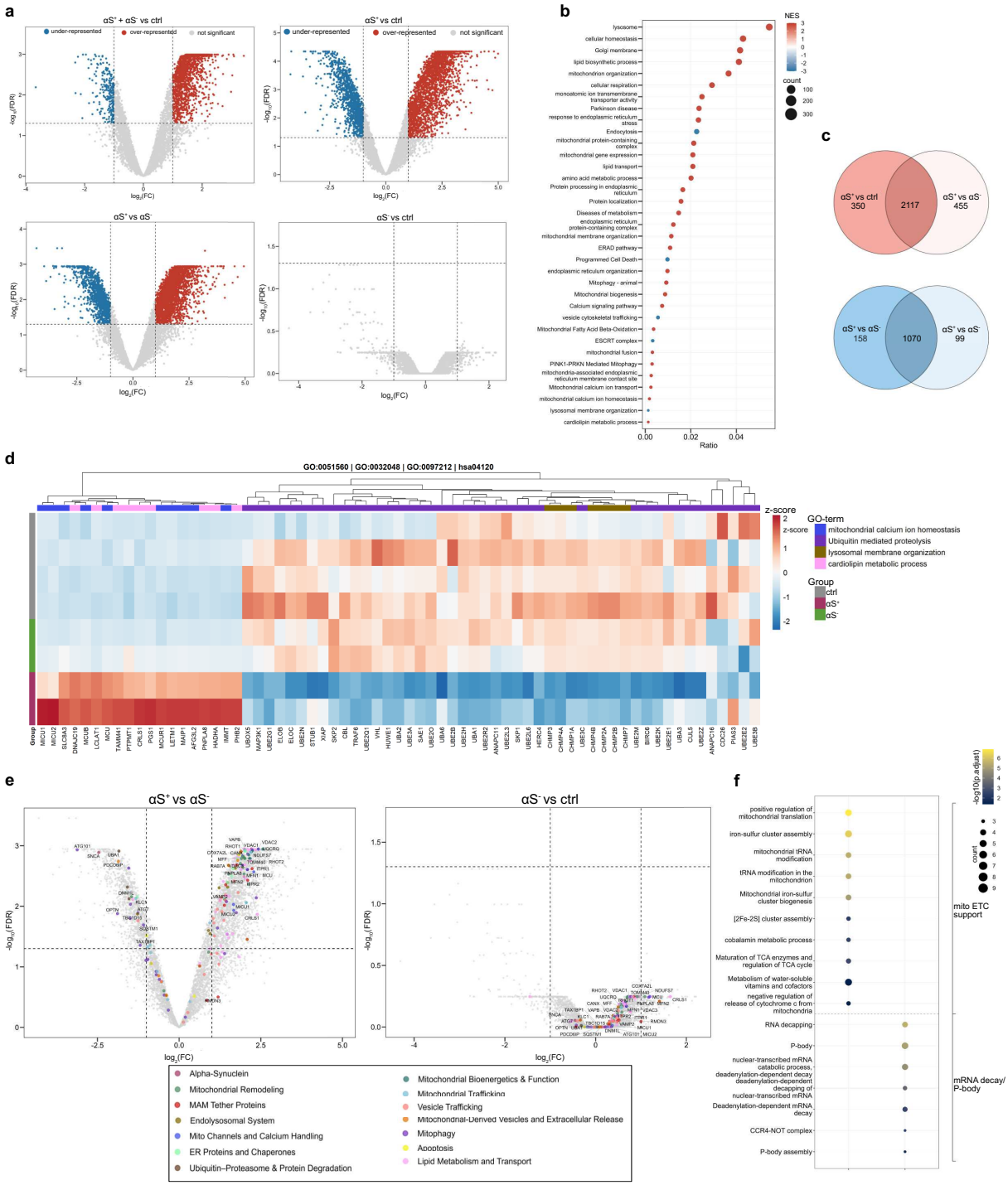

Figure S3. Differential proteomic changes and pathway stratification across αS–defined mitochondrial populations.

a, Volcano plots showing differentially abundant proteins across all pairwise comparisons: combined αS-treated mitochondrial populations ($αS^+ + αS^-$) vs ctrl, $αS^+$ vs ctrl, $αS^+$ vs $αS^-$, $αS^-$ vs ctrl. Proteins are colored to indicate over-representation (red), under-representation (blue), or no significance (gray). Volcanoes illustrate global proteomic changes induced by αS exposure, which is absent in $αS^-$ vs ctrl.

b, GSEA of pooled mitochondrial populations from αS-treated cells ($\alpha S^+ + \alpha S^-$) vs ctrl. Enriched pathways include mitochondrial organization, respiration, lipid metabolism, and ER stress, whereas trafficking and transport terms are depleted.
c, Venn diagrams showing overlap of differentially expressed proteins across comparisons. Top: overlap of overrepresented proteins. Bottom: overlap of underrepresented proteins.
d, Heatmap of selected enriched pathways across ctrl, αS^-, and αS^+. Hierarchical clustering reveals distinct pathway signatures, with αS^+ mitochondria enriched in mitochondrial calcium homeostasis and lipid metabolism and depleted in ubiquitin-mediated processes.
d, ORA of unique pathways distinguishing αS^+ vs ctrl and αS^+ vs αS^- comparisons. Dot plot highlights pathways selectively enriched or depleted in αS^- vs ctrl.
e, Volcano plots for: top, αS^+ vs ctrl; middle, αS^+ vs αS^-; bottom, αS^- vs ctrl. These comparisons illustrate the magnitude of proteomic changes in αS^+ mitochondria relative to both control and αS^-, and the comparatively limited changes in αS^- vs ctrl.
f, Volcano plots comparing αS^+ vs αS^- (left) and αS^- vs ctrl (right) mitochondrial fractions. Proteins of interest are highlighted and grouped into custom-defined functional categories, whereas all other differentially abundant proteins are shown in grey. Annotated proteins are referenced in the Results section. Dashed lines indicate significance thresholds (adjusted $p < 0.05$; $|\log_2 FC| > 1$).
A table listing proteins of interest and their assigned functional categories is provided below (Supplementary Table S1). Statistical significance was determined using the false discovery rate (FDR) correction, further described in the Methods. Biological replicates, ctrl, αS, N=4; αS_D, N=2.

Figure 4

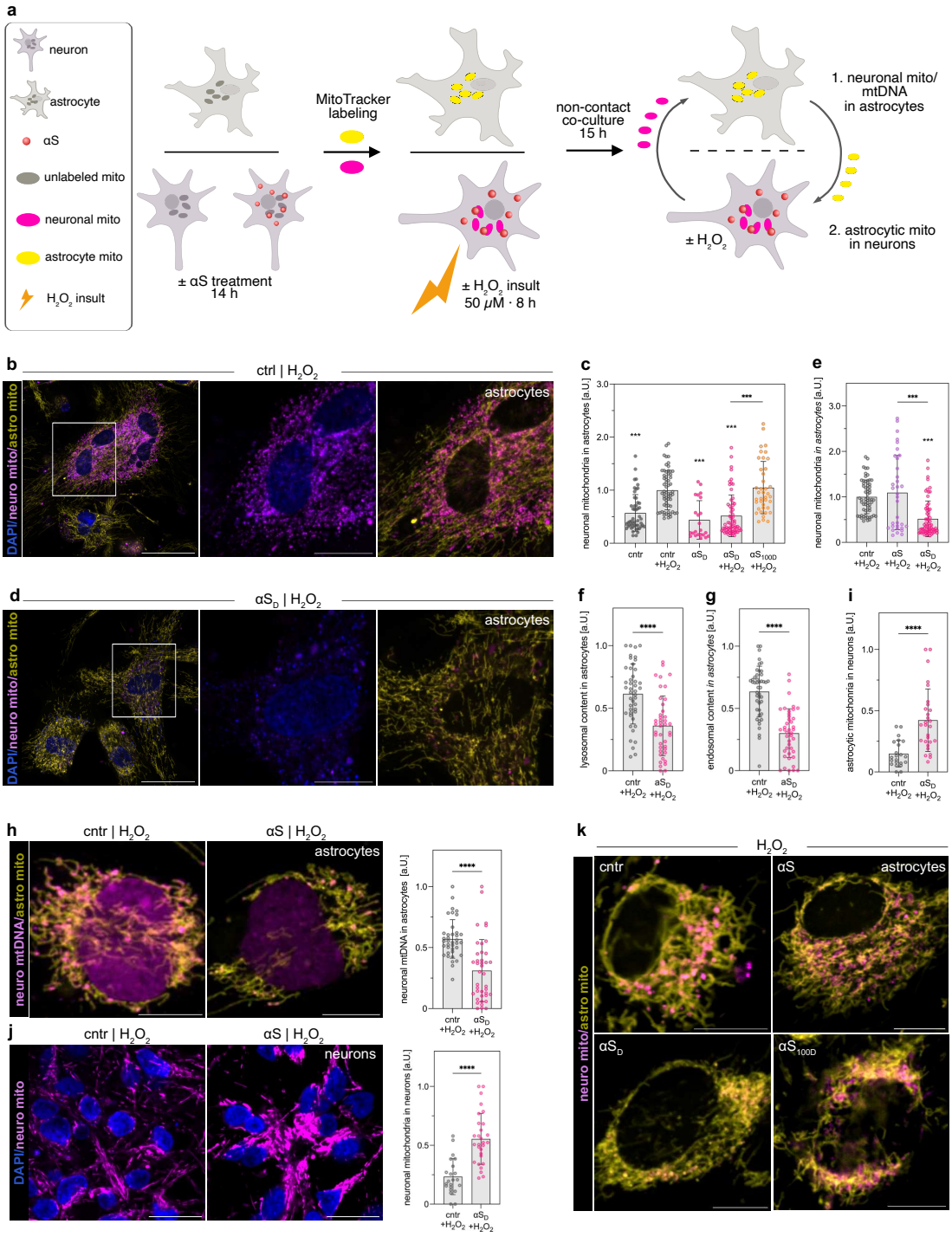
a
neuron
astrocyte
αS
unlabeled mito
neuronal mito
astrocyte mito
H2O2 insult
± αS treatment 14 h
MitoTracker labeling
non-contact co-culture 15 h
1. neuronal mito/ mtDNA in astrocytes
2. astrocytic mito in neurons
± H2O2
± H2O2 insult 50 μM · 8 h
b
ctrl | H2O2
DAPI/neuro mito/astro mito
astrocytes
c
neuronal mitochondria in astrocytes [a.U.]
cntr
cntr +H2O2
αSD +H2O2
αS100D +H2O2
d
αSD | H2O2
e
neuronal mitochondria in astrocytes [a.U.]
αS +H2O2
f
lysosomal content in astrocytes [a.U.]
g
endosomal content in astrocytes [a.U.]
i
astrocytic mitochondria in neurons [a.U.]
h
cntr | H2O2
αS | H2O2
neuro mtDNA/astro mito
neuronal mtDNA in astrocytes [a.U.]
j
neurons
DAPI/neuro mito
neuronal mitochondria in neurons [a.U.]
k
H2O2
cntr
αS
αSD
αS100D
neuro mito/astro mito

Figure 4. Spreading αS disrupts neuron-to-astrocyte mitochondrial transfer and alters intercellular mitochondrial exchange.

a, Schematic of the non-contact neuron–astrocyte co-culture used to assess bidirectional mitochondrial transfer. Neuronal mitochondria (magenta), astrocytic mitochondria (yellow), and αS (red) are shown.

b, Representative images of astrocytes under H_2O_2 conditions showing uptake of neuronal mitochondria (neuro mito: magenta) into astrocytic cells (astro mito: yellow). Insets highlight transferred mitochondria.

c, Quantification of neuronal mitochondria detected in astrocytes under basal and oxidative stress (H_2O_2) conditions, in the presence or absence of αS_D or αS_{100D}. LMM with random intercept (1|Replicate), Tukey HSD post-hoc on estimated marginal means, lmerTest/emmeans. *N*=2-4 biological replicates.

d, Quantification of early endosomal intensity (Rab5) in astrocytes, following neuronal mitochondrial transfer to astrocytes under stress conditions.

e, Quantification of lysosomal intensity (Lamp1) in astrocytes, following neuron-astrocyte mitochondrial transfer under stress conditions. d, and e, Unpaired two-tailed Welch's t-test; *N*=3 biological replicates.

f, Representative images of astrocytes co-cultured with αS-treated neurons under H_2O_2 conditions, showing reduced neuronal mitochondria signal in astrocytes.

g, Quantification of neuronal mitochondrial uptake by astrocytes in control and αS-treated conditions, demonstrating a significant reduction in transfer upon αS exposure in a concentration-dependent manner. Statistics as stated in c.

h, Representative images and quantification of neuronal mtDNA (denoted neuro mtDNA: magenta) detected within astrocytes, confirming reduced transfer of neuronal mitochondrial material upon αS_D treatment. Unpaired two-tailed Mann-Whitney. *N*=2 biological replicates.

i, Quantification of astrocyte-to-neuron mitochondrial transfer, showing increased transfer of astrocytic mitochondria into neurons upon αS exposure. Two-tailed Welch's t-test; *N*=3 biological replicates.

j, Representative images and quantification of neuronal mitochondria in control and αS-treated neurons upon stress. Statistics as stated in i.

k, Representative images comparing neuronal mitochondria signal in astrocytes following neuronal-to-astrocyte mitochondrial transfer. αS_{100D} does not reproduce the effect of αS_D on mitochondrial transfer.

Data are mean ± s.e.m.; each point represents one cell or FOV. *P < 0.05, **P < 0.01, ***P < 0.001, ****P < 0.0001. Values were normalized to the within-replicate ctrl+H_2O_2 mean. Filled symbols: no insult; open symbols: +H_2O_2. Scale bars: c, f, 50 µm; insets, 20 µm; h, j, k, 10 µm.

Figure S4

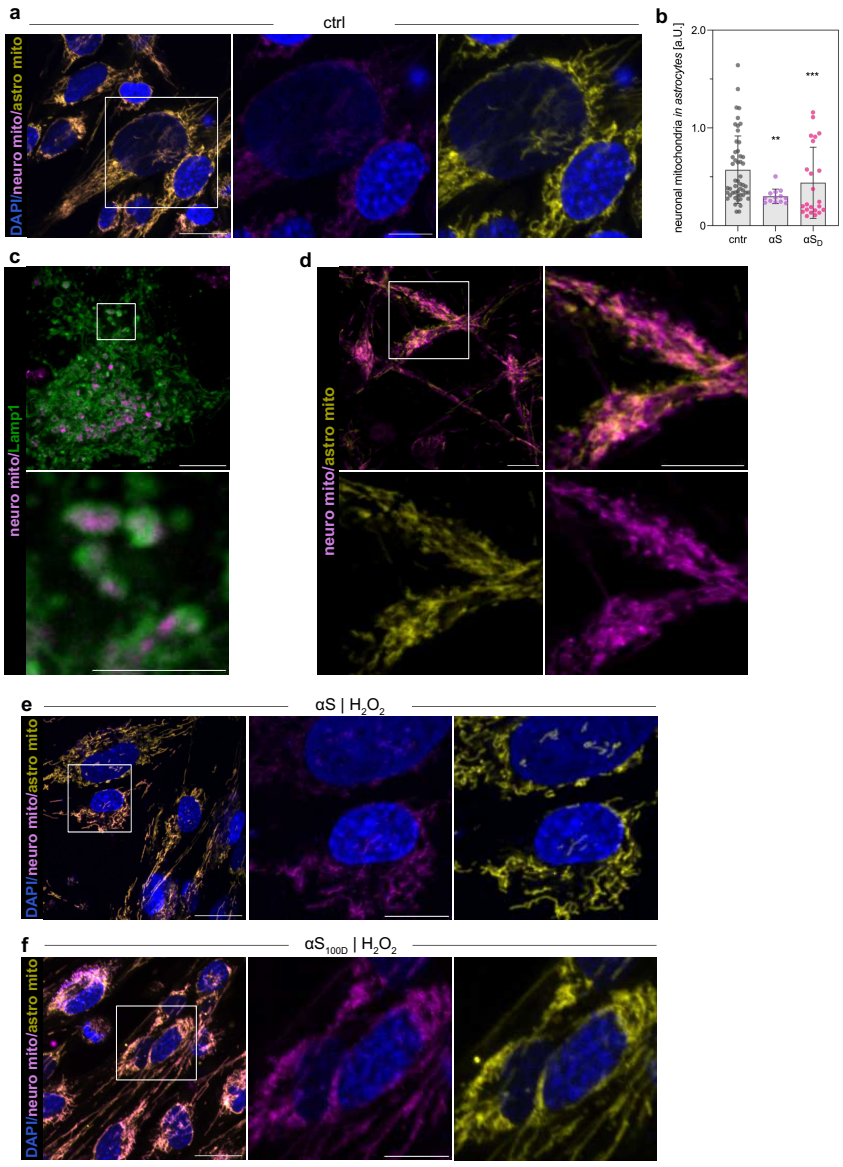

Figure S4. αS impairs neuronal mitochondrial transfer and lysosomal processing.

a, Representative confocal images of astrocytes co-cultured with neurons under basal conditions, showing detectable uptake of neuronal mitochondria (denoted neuro mito: magenta) into astrocytes (denoted astro mito: yellow). Insets highlight transferred mitochondria content.

b, Quantification of a, neuronal mitochondrial transfer to astrocytes under basal conditions. αS presence in neurons significantly reduces mitochondrial transfer to astrocytes compared with controls. LMM with random intercept (1|Replicate), Tukey HSD post-hoc on estimated marginal means, lmerTest/emmeans. *N*=2 biological replicates.

c, High-resolution images showing neuronal mitochondria (magenta) localized within Lamp1-positive lysosomal compartments (green) in astrocytes, indicating delivery of transferred neuronal mitochondria to degradative organelles.

d, Representative images of the neuronal portion of co-cultures. Images suggest the incorporation of astrocytic mitochondrial signal (yellow) into the neuronal mitochondrial network (magenta).
e, f, Representative images of astrocytes co-cultured with αS and $αS_{100D}$-treated neurons under oxidative stress. Neuronal mitochondrial signal (magenta) illustrates neuron-to-astrocyte mitochondrial transfer.
Data are mean ± s.e.m.; each point represents one cell or FOV. * $p < 0.05$, ** $p < 0.01$, *** $p < 0.001$. Values normalized to within-replicate ctrl+H_2O_2 mean. Filled markers: no insult; open markers: +H_2O_2. Scale bars: a, c, e, f 20 µm; d, insets a, e, f 10 µm, inset c, 2.5 µm.

Supplementary Files

This is a list of supplementary files associated with this preprint. Click to download.

- MovieS2.mp4
- MovieS1.mp4
- SupplementaryTableS1.xlsx
- MovieS4.mp4
- MovieS3.mp4